Marine and Petroleum Geology 143 (2022) 105781

Contents lists available at ScienceDirect

Marine and Petroleum Geology

journal homepage: www.elsevier.com/locate/marpetgeo

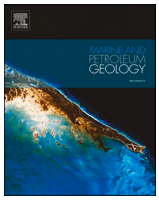

Pore system evolution in arenaceous regoliths - Case study from the Sila Massif (southern Italy)

Lars Riber [a,*], Emilia Le Pera [b], Consuele Morrone [b], Fabio Ietto [b], Massimo Conforti [c], Henning Dypvik [a,d]

[a] Department of Geosciences, University of Oslo, Norway
[b] Department of Biology, Ecology and Earth Sciences, University of Calabria, Italy
[c] National Research Council of Italy—Research Institute for Geo-Hydrological Protection (CNR-IRPI), Via Cavour 4/6, 87036, Rende, Cosenza, Italy
[d] Department of Technology Systems, University of Oslo, Norway

A B S T R A C T

Porous and permeable crystalline rocks have the potential of being hydrocarbon reservoirs. In many cases, reservoir properties are created by rock-altering physico-chemical processes occurring in the near-surface environment. Hydrocarbon reservoirs in altered granitoids may comprise both arenaceous (clay-poor) and argillaceous (clay-rich) palaeoregoliths, and hence outcrop analogues from various environments are required. In the Sila Massif, southern Italy, the arenaceous weathering of medium to coarse grained granodioritic rocks has been studied. The pore system, dominated by microfractures, was described and quantified at each stage in the weathering process (altered coherent rock facies → saprock facies→ lower and upper saprolite facies → soil) in relation to changes in chemical and physical properties. The transformation of rock to saprolite was close to an isochemical process, as demonstrated by the low variations in the bulk mass transfer coefficient (τ_{bulk}). At the same time, trans-, intra- and intermineral microfractures increased in frequency and aperture upwards through the regolith profile. It was the main reason for the reduction of bulk densities (ρ_b) from 2.66 g/cm^3 in the altered coherent rock to 1.88 g/cm^3 in the saprolite, corresponding to the formation of up to 30% porosity (φ_c). The results suggest that a volume increase of >50%, represented by the volumetric strain factor (ε), was the main cause for the transformation of solid crystalline rock to porous saprolite. Anisovolumetric arenaceous regoliths with minimal mass loss, are the result of one of the major weathering processes, notwithstanding that they are much less understood than isovolumetric, anisochemical, argillaceous regoliths. Arenaceous saprolites potentially can have excellent porosity and permeability properties, with open and well-connected microfractures. Reservoir quality of arenaceous saprolites is in stark contrast to the poor permeability observed in some argillaceous saprolites where porosity is dominated by isolated dissolution voids within a clay-rich matrix.

1. Introduction

Fault-controlled basement highs in mature sedimentary rift basins have successfully been targeted in petroleum exploration in e. g the Cuu Long Basin, Vietnam (Areshev et al., 1992; Cuong and Warren, 2009), Qaidam Basin, China (Yang et al., 2020), Gulf of Suez Rift, Egypt (Salah and Alsharhan, 1998; Braathen et al., 2018) and Say'un Masila Basin, Yemen (Legrand et al., 2011; Murray and Montgomery, 2014). Recent discoveries in the North Sea, along the Rona Ridge, West of Shetland (Trice et al., 2019) and on the Utsira High, Norway (Riber et al., 2015, 2016, 2017, 2019; Lie et al., 2016; Fredin et al., 2017; Rønnevik et al., 2017; Lothe et al., 2018; Ottesen et al., 2022), have initiated the search for similar basement plays on the Norwegian and UK continental shelves (Trice et al., 2019).

Crystalline basement reservoirs may exhibit a layered architecture comprising a fractured rock layer below a zone of regolith (Dewandel et al., 2006; Cuong and Warren, 2009; Lachassagne et al., 2011; Braathen et al., 2018; Novitsky et al., 2018). The reservoir potential of initially tight crystalline rocks is dependent on secondary processes creating porosity and permeability (Nelson et al., 2000; Gutmanis, 2009; Le Van Hung et al., 2009). Crystalline rock reservoirs are dual porosity systems (Abdelazim and Rahman, 2016). The capacity to store and transport fluids may be improved by a combination of tectonically induced fractures and joints (Sausse and Genter, 2005; Pacheco and Alencoão, 2006; Rossi and Graham, 2010; Novitsky et al., 2018), and the creation of matrix pores through physico-chemical alteration processes (Vepraskas et al., 1996; Graham et al., 1997; Schild et al., 2001; Navarre-Sitchler et al., 2013, 2015; Santos et al., 2018).

In the fractured layer, matrix porosity is low (<1%) and permeable fractures are the preferential conduits for fluid flow (Boutt et al., 2010; Lachassagne et al., 2011; Braathen et al., 2018; Nara et al., 2011). In the overlying regolith, matrix porosity may increase upwards due to physico-chemical alteration that occurred in the near-surface environment (Wright, 1992; Velde and Meunier, 2008; Braathen et al., 2018).

* Corresponding author.
E-mail address: lars.riber@geo.uio.no (L. Riber).

https://doi.org/10.1016/j.marpetgeo.2022.105781
Received 12 February 2022; Received in revised form 2 June 2022; Accepted 6 June 2022
Available online 13 June 2022

Arenaceous weathering is a particularly effective weathering process that transforms solid crystalline rocks into highly porous and permeable material, composed of a network of interconnected microfractures. The low to intermediate grade of chemical alteration and minimal transfer of mass are features that set arenaceous weathering apart from weathering processes resulting in clay-rich material (argillaceous weathering) (Środoń, 1999; Begonha and Sequeira Braga, 2002; Sequeira Braga et al., 2002; Riber et al., 2017). The resulting product, arenaceous saprolite (also called grus/growan/arène), is the result of *in-situ* aniso-volumetric weathering of parent rock into a coarse-grained saprolite. The combined silt and clay content is typically <25%, clay content alone is <10% and the chemical index of alteration (CIA) is generally 60–70 (Sequeira Braga et al., 1990, 2002; Migoń and Thomas, 2002; Parizek and Girty, 2014).

Recent studies have highlighted the importance of anisovolumetric weathering processes, and how porosity is created in such saprolites by dilation, forming a network of interconnected microfractures (e.g. Parizek and Girty, 2014; Hayes et al., 2019; Riebe et al., 2021). Arenaceous saprolites stand in contrast to their argillaceous counterparts, that retain the original rock volume and where porosity mainly forms as a result of mineral dissolution, clay precipitation and the transfer of mobile cations (Brimhall and Dietrich, 1987; Stolt and Baker, 1994; Soil Science Glossary Terms Committee, 2008).

Arenaceous saprolites are present across all climate zones, but are typically formed on coarse grained and weathering-prone lithologies in tectonic regimes characterised by rapid uplift and continuous removal of newly formed regolith, where tectonically induced fractures and increased relief promote easy ingress for water (Migoń and Lidmar-Bergström, 2001; Migoń and Thomas, 2002).

Difficulties in collecting undisturbed samples of unconsolidated saprolites from drill cores (Cuong and Warren, 2009), and the fact that complete palaeoregolith profiles rarely are preserved in the rock record (Thiry et al., 1999; Migoń and Thomas, 2002), have initiated the search for adequate outcrop analogues to examine the formation of pores at each weathering stage. In this study, we have investigated the weathering of granodioritic rocks under a Mediterranean type of climate in the Sila Massif, Calabria region of southern Italy (Fig. 1).

In a previous study in the same location, Perri et al. (2015) described and reconstructed the weathering processes by mineralogy, chemistry and reaction path modelling. Therefore, the present paper focuses on describing and quantifying pore formation in relation to the physico-chemical processes at different stages in the arenaceous weathering of granodiorites in the Sila Massif. The pore-forming mechanisms were studied by combining multiple parameters such as physical properties (density), proportions of individual mineral alteration, changes in composition, amount of secondary material formed and the flux of mobile elements.

This study aims to increase our understanding of how microfractures form in the near-surface environment and the importance of microfractures for fluid flow and storage capacities in crystalline rocks. In addition to having the potential of being unconventional hydrocarbon reservoirs, fractured and weathered crystalline rocks may form important aquifers in areas where access to clean drinking water is otherwise limited (e.g. Jones, 1985; Acworth, 1987; George, 1992; Wright, 1992; Chilton and Foster, 1995; Foster, 2012). However, incomplete understanding of the hydraulic conductivity of such systems may result in the misplacement of wells or reduced yields (Lachassagne et al., 2021; Njueya et al., 2022). Moreover, as the exploitation of geothermal energy, in the absence of volcano-derived hydrothermal activity and high heat flow, is expanding worldwide, plutonic provinces and permeable geothermal reservoirs in granitic plutons studies, have led to a breakthrough in the field of geothermal resources (e.g. Ebigbo et al., 2016; Farquharson et al., 2020; Klee et al., 2021). Specifically, fractured granites, provide space and pathways for the storage and migration of

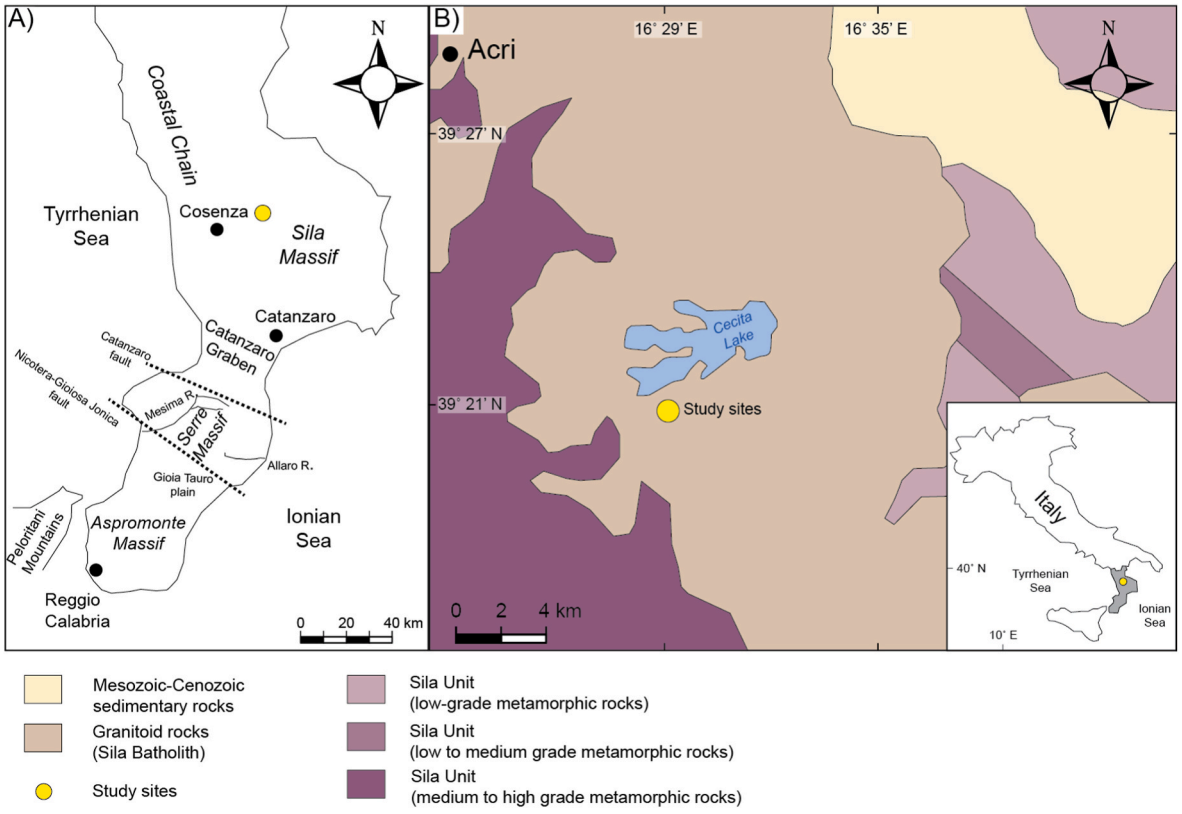

Fig. 1. A) Map of the Sila Mountains showing the position of the study sites (yellow circle) and main tectonic units from the Sila Massif. B) Map showing the study sites and the main lithostratigraphic units from the Sila Massif. Modified from Messina et al., 1991; Borrelli et al., 2014; Perri et al., 2015. (For interpretation of the references to colour in this figure legend, the reader is referred to the Web version of this article.)

geothermal fluids (e.g. Zheng et al., 2021).

2. Geological setting

The study sites are located in the Sila Massif (Calabria, southern Italy) (Fig. 1) that falls within the Calabrian Arc on the broad collisional boundary between the European and African tectonic plates (Faccenna et al., 2001). The Calabrian Arc (Amodio-Morelli et al., 1976), part of the Mediterranean orogenic belt, represents an accretionary wedge consisting of Alpine units made up of ophiolite-bearing tectonic segments and of overlying basement nappes (Tansi et al., 2016 and references therein). The Calabrian microplate rifted off the southern margin of the European plate and drifted southeastward, overthrusting the northern margin of the African plate during the Neogene (Critelli and Le Pera, 1998; Van Dijk et al., 2000). The subduction zone of the Calabrian Arc is a turning point along the roughly E-W Eurasian-African plate boundary in the Central Mediterranean (Maesano et al., 2017). Following the latest deformation phase, a late Pleistocene to recent destabilisation episode has resulted in the area being highly active, seismically and volcanically (Van Dijk and Scheepers, 1995). The Calabrian Arc is composed of three structural sectors: the Sila, Serre and Aspromonte massifs (Amodio-Morelli et al., 1976) (Fig. 1A).

The Sila Massif is a batholith within the northern sector of the Calabrian Arc (Fig. 1B). The Sila Massif has experienced rapid uplift of 0.8–1.1 mm/y since the Quaternary (Westaway, 1993). The metamorphic and plutonic terranes of the Sila Massif consist of Palaeozoic intrusive and metamorphic rocks, locally with a Mesozoic unmetamorphosed cover (Amodio-Morelli et al., 1976; Messina et al., 1991) (Fig. 1B). The plutonic rocks of the Sila Massif, ranging in composition from granodiorite to gabbro and leucomonzogranite, crop out over about 900 km^2. Fission track analysis has revealed the main period of exhumation was between ~35 and ~15 Ma (Thompson, 1994). From a morphological perspective the Sila Massif is characterised by highlands consisting of paleosurfaces, ranging in height from about 1000 to 1700 m a.s.l. and gently rolling hills strongly controlled by WNW-ESE and NE-SW trending joints and faults. This landscape is dissected by deep incisions and bordered by steep slopes, where there is evidence of widespread erosion and mass wasting. In some places, especially on the residual paleosurfaces where the regolith has been removed, subspherical corestones and boulders of unweathered or less weathered rock crop out (Scarciglia et al., 2005, 2007).

Weathering in the Sila Massif have probably developed under Mediterranean climate during Pleistocene (Le Pera and Sorriso-Valvo, 2000). Weathering of crystalline rocks in the Calabria region have resulted in the transformation of fresh bedrock to arenaceous saprolites (Mongelli et al., 1998; Le Pera and Sorriso-Valvo, 2000; Le Pera et al., 2001; Scarciglia et al., 2005; Borrelli et al., 2012; Perri et al., 2016; Biondino et al., 2020). Depending on the degree of erosion, the depth of surviving weathering profiles ranges from 1 up to 100 m (Le Pera and Sorriso-Valvo, 2000; Scarciglia et al., 2005).

Weathering of felsic igneous rocks (tonalites, granodiorites, granites) results is a mantle of unconsolidated regolith in which sand is the main grain-size fraction, on both the Sila (e.g. Le Pera and Sorriso-Valvo, 2000) and Serre massifs (e.g. Moresi, 1987) (Fig. 1A).

3. Material and methods

3.1. Study sites and macromorphology

The study sites (Figs. 1 and 2A) are in an abandoned quarry where weathered granodiorite of the Sila Massif crops out in a >35 m thick regolith profile (Fig. 2B). The degree of weathering was determined using a visual scale from W1 – W5 reflecting changes in colour, texture, hardness or shape with increased weathering (Stoops et al., 1979), as observed in the field. Based on the degree of weathering, the regolith profile was subsequently divided into three distinct weathering facies (altered coherent rock (ACR), saprock, and (lower and upper) saprolite facies) (Meunier et al., 1983; Velde and Meunier, 2008; Stoops et al., 2010; Riber et al., 2017) in addition to the superjacent soil horizons (Fig. 2C).

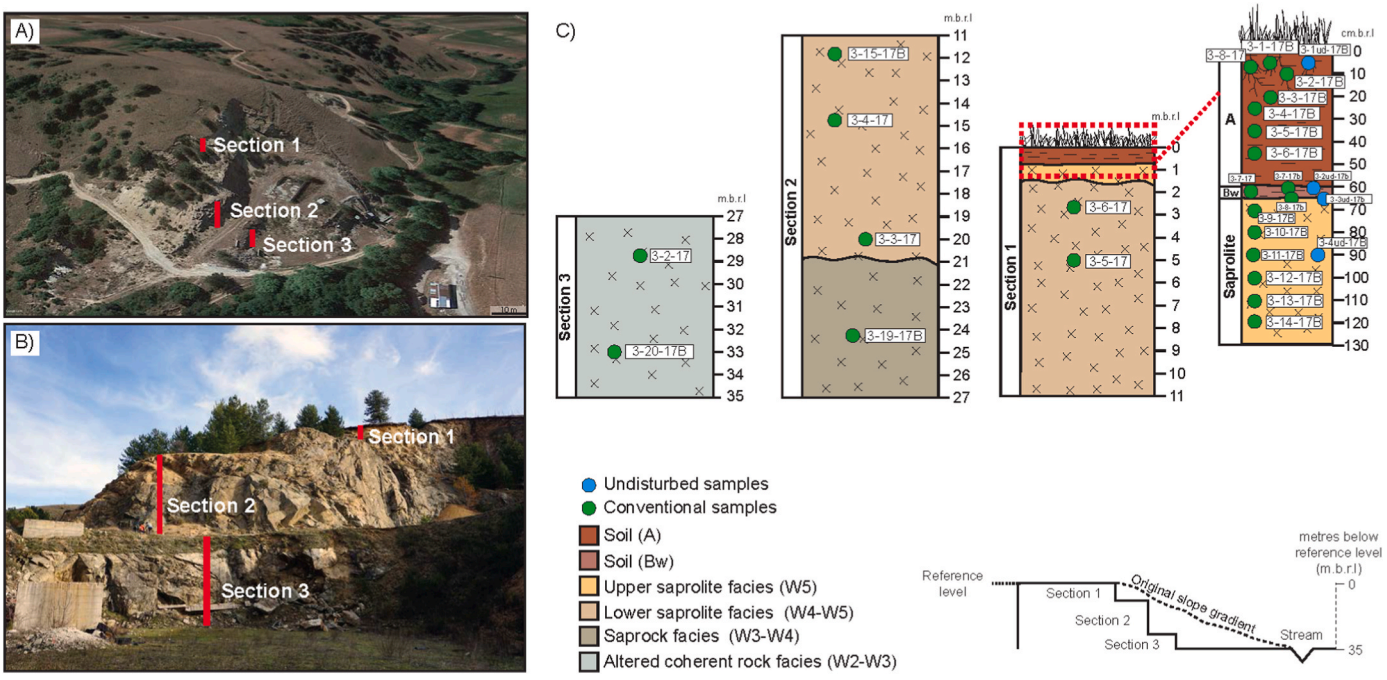

Fig. 2. A) Satellite image (GOOGLE EARTH) of outcrops studied, oblique view looking SW.
B) Image of outcrop and subdivision into three sections. (39° 21′ 41″ N, 16° 29′ 37″ E).
C) Sketch log from outcrop with sample positions marked in relation to weathering facies (altered coherent rock, saprock, lower and upper saprolite facies) and soil horizons (Bw and A). The degree of weathering (W1 – W5) is noted.

3.2. Sampling

Twenty-five conventional rock samples, representing distinct weathering facies and soil horizons, were collected. Selected samples were picked out for petrographical, mineralogical and geochemical analyses (Fig. 2C). In addition, four undisturbed samples of saprolite and soil material were obtained, from corresponding levels, with push corer equipped with stainless steel soil sample rings (https://eijkelkamp.com, product code 07.01.53. NN) in order to acquire accurate density measurements (Table 1) and produce thin sections with preserved fabric from the incoherent saprolite and soil intervals (Fig. 2C).

3.3. Petrography

Eleven polished thin sections, impregnated with blue epoxy to highlight pore space, were prepared and analysed at the Department of Geosciences, University of Oslo, using a Nikon Labophot-Pol polarizing optical microscope, equipped with PELCON automatic point counter. Dependent on the area of the thin section, 300–400 points were counted for each slide (Table 2).

3.3.1. Single minerals and degree of alteration and pores

Every mineral phase beneath the crosshairs was counted according to categories in Table 2 and then assigned to a degree of alteration following the guidelines by Stoops et al. (1979) (Fig. 6). These give five classes of alteration, based on the amount of transformation to secondary material attributable to weathering: fresh-nearly fresh (<2.5% transformed to secondary material), slightly altered (2.5–25% transformed), moderately altered (25–75% transformed), strongly altered (75–97.5% transformed), and completely altered (>97.5% transformed).

In this relation, it should be mentioned that chloritised biotite might be a product of late-stage weathering (Stoch and Sikora, 1976), but most authors consider biotite chloritisation and also sericitiation of plagioclase to have a metasomatic origin (Parneix et al., 1985; James et al., 1981; Que and Allen, 1996; Wilamowski, 2002; Stoops et al., 2010). Therefore, the products of these two processes were not included within the secondary weathering materials in this study.

Fine-grained material in the form of infillings of FeOx and clay coatings were counted individually. In samples from the soil horizons, fragments of organic material, soil aggregates and rounded rock fragments were counted as separate categories (Table 2).

High-magnification images for micromorphological interpretation and chemical composition were obtained from selected samples on a Hitachi SU5000 FE-SEM (Schottky FEG) scanning electron microscopy (SEM) with a Dual Bruker XFlash30 Energy Dispersive X-ray Spectroscopy (EDS) system at the Department of Geosciences, University of Oslo.

3.3.2. Porosity

Every counted void was either classified as pores, caused by the partial dissolution of the parent mineral, or as microfractures (elongated pores). The latter occurred in three varieties: intramineral (within a mineral grain), transmineral (cutting across two or more mineral grains, not following grains boundaries), or intermineral (following grain contacts) (Bisdom, 1967; Delvigne, 1998; Mazurier et al., 2016) (Table 2). Furthermore, pores were categorised either as open, including those coated by veneers of clay along the fracture wall, or as closed by neoformed or transported products (Stoops et al., 1979) (Table 2).

3.3.3. Crystal interfaces

Three thin sections were prepared at the Department of Biology, Ecology and Earth Sciences, University of Calabria, from unsieved saprolite and soil samples (samples 3-5-17; 3-7-17; 3-8-17). The samples were subsampled using a splitter, washed with H_2O_2 to remove clay minerals and organic matter, air-dried and then impregnated with epoxy resin. Thin sections were then etched with hydrofluoric acid to allow identification of plagioclase feldspars (Bailey and Stevens, 1960). In addition, eight thin sections, prepared at the University of Oslo, were included in the study of crystal interfaces (Tables 3 and 4).

For the measurement procedure of interface types in Table 3, each thin section was moved, using a mechanical stage, counting the interface types for 100 grains. For every grain, the interface between isomineralic or anisomineralic crystals were identified and counted under the polarizing microscope (Table 4) (Heins, 1995; Le Pera and Morrone, 2020). The number of counted interfaces ranged from a minimum value of 148 (sample 3-8-17) to a maximum of 500 interfaces (samples 3-4-17, 3-3-17, 3-2-17) (Table 4).

Petrographic data of analysed plutoniclastic detritus included compositional counts to determine interface type and frequency (Table 4) in order to characterise rate and style of comminution in relation to crystalline interfaces of plutoniclastic grains (e.g. Heins, 1993, 1995) in a modern arenaceous saprolite environment. The use of mineral interfaces, determined for plutoniclastic sand-sized rock fragments, has previously received attention as a method to infer the influence exerted by durability on the generation of siliciclastic sediments (e.g. Palomares and Arribas, 1993; Heins, 1995; Caracciolo et al., 2012; Weltje et al., 2018).

Isomineralic interfaces are those between crystals of the same mineral such as Qz/Qz (Quartz/Quartz), Kfs/Kfs (K-feldspar/K-feldspar) and Pl/Pl (Plagioclase/Plagioclase) (Table 4). Anisomineralic interfaces are boundaries between crystals of different minerals. Anisomineralic

Table 1
Laboratory analysis and calculated parameters of undisturbed soil and saprolite samples collected by push corer.

Sample	Corresponding conventional sample[a]	Facies	Wt. (wet)	Wt. (dry)	Wt. (ring)	Wt. regolith[b]	V. ring	ρ_b[c]	Water[d]	φ_{calc}[e]
3-1UD-17B	3-1-17B	Soil (A)	234.70	210.20	95.12	115.08	100	1.15	12	57
3-2UD-17B	3-7-17B	Soil (Bw)	281.30	253.80	92.62	161.18	100	1.61	11	39
3-3UD-17B	3-8-17B	Sapr (U)	299.30	281.00	92.74	188.26	100	1.88	7	29
3-4UD-17B	3-11-17B	Sapr (U)	299.70	270.60	92.69	177.91	100	1.78	11	33

Explanation of abbreviations.
Facies: Soil (A): soil A horizon, Soil (Bw): Soil Bw-horizon, Sapr (U): upper saprolite facies.
Wt.: weight reported in g, V.: volume reported in cm3.

[a] Undisturbed samples were obtained from same levels as corresponding conventional samples used for XRD and XRF. See also Fig. 2 for sample positions.

[b] Weight of the regolith $Wt.\,regolith = Wt.\,(dry) - Wt.\,(ring)$.

[c] Bulk density (ρ_b): $\rho_b = \frac{Wt.\,regolith}{V.\,ring}$ g/cm^3.

[d] Water content: $Water = 100 \times \frac{Wt.\,(wet) - Wt.\,(dry)}{Wt.\,(dry)}$ %.

[e] Calculated porosity (φ_{calc}): $\varphi_{calc} = 100 \times \left(1 - \frac{\rho_b}{\rho_g}\right)$%, assuming grain density (ρ_g) of 2.66 g/cm^3.

Table 2
Quantitative petrographical results in % from point counting of selected regolith samples.

Sample	Facies	Single minerals							Fine-grained		Soil constituents			Voids							Tt
		Qz	Pl	Mc	K-fsp	Ms	Bt	Acc.	FeOx	Ct	Org	Soil	Rf	Pores		Intermin		Intramin		Transmin	
														Op	Cl	Op	Cl	Op	Cl	Op	Cl	
3-1UD-17B	Soil (A)	14.0	11.7	6.0	0.0	1.00	2.3	1.0	0.0	3.3	2.3	25.0	4.3	28.0	0.0	0.0	0.0	0.0	0.7	0.0	0.3	100
3-2UD-17B	Soil (Bw)	21.0	23.0	10.3	0.0	0.30	5.0	0.0	0.0	4.0	0.3	11.0	0.0	23.3	0.7	0.0	0.0	0.0	0.0	0.3	0.7	100
3-3UD-17B	Sapr (U)	29.2	23.7	5.2	11.7	0.90	5.2	0.0	0.0	1.5	0.0	0.0	0.0	3.7	2.3	5.2	2.0	0.4	0.9	5.7	2.7	100
3-10-17B	Sapr (U)	38.5	20.2	5.0	17.8	0.00	5.0	0.0	0.8	0.5	0.0	0.0	0.0	2.0	0.2	2.0	0.5	0.8	0.5	4.5	1.8	100
3-4UD-17B	Sapr (U)	36.0	6.8	0.8	20.0	0.80	9.5	0.0	0.5	0.8	0.0	0.0	0.0	5.8	11.0	1.8	0.5	0.8	0.8	4.0	0.5	100
3-11-17B	Sapr (U)	44.0	14.2	8.2	14.0	3.00	7.2	0.0	0.5	0.8	0.0	0.0	0.0	0.5	0.2	1.5	1.5	0.2	1.2	1.8	1.0	100
3-13-17B	Sapr (U)	34.0	13.5	9.0	18.5	0.80	6.5	0.0	0.0	1.2	0.0	0.0	0.0	0.0	0.0	4.0	0.8	0.0	0.8	9.2	1.8	100
3-14-17B	Sapr (U)	44.8	17.8	6.0	12.0	0.20	7.0	0.0	0.5	1.0	0.0	0.0	0.0	2.2	0.2	2.0	0.2	0.0	0.5	3.2	2.2	100
3-15-17B	Sapr (L)	30.9	28.8	11.0	7.4	1.65	6.9	0.0	0.6	1.2	0.0	0.0	0.0	0.7	0.1	2.2	0.0	0.3	1.0	5.7	1.9	100
3-19-17b	Saprock	17.7	35.1	15.0	14.6	2.35	8.5	0.0	0.0	0.1	0.0	0.0	0.0	0.4	0.0	0.4	0.6	0.5	1.1	3.3	0.5	100
3-20-17B	ACR	37.0	25.7	6.4	17.5	1.75	7.6	0.0	0.1	0.0	0.0	0.0	0.0	0.4	0.1	0.6	0.8	0.	0.9	0.2	0.5	100

Explanation of abbreviations.
Facies: Sapr (U): upper saprolite facies, Sapr (L): lower saprolite facies, ACR: altered coherent rock facies.
Point counting categories.
Single minerals: Qz: quartz Pl: plagioclase feldspar (as determined by optical characteristics and cross-checked by SEM) Mc: microcline feldspar (as determined by optical characteristics such as tartan twinning and cross-checked by SEM) Kfs: K-feldspar (as determined by intergrowths of perthites and cross-checked by SEM) Ms: muscovite Bt: biotite, including chloritised biotite (as determined by optical characteristics)Acc: accessories (all minerals not in included in one of the other categories).
Fine-grained: FeOx: iron oxides, Ct: coating on fracture walls.
Soil constituents: Org: organic material, Soil: soil aggregate, Rf: rock fragment of unknown origin.
Pores: Intermin: intermineral microfracture, Intramin: intramineral microfracture, Transmin: transmineral microfracture, Op: open, Cl: closed, Tt: total.

interfaces can be either with strongly contrasting crystal structures (anisomineralic anisostructural) such as Qz/Opq (Quartz/Opaque) (Table 4), or with identical crystal structures (anisomineralic isostructural) such as Qz/Pl or Qz/Kfs (Table 4).

The petrographic analysis of thin sections was used to determine the nature of the crystal/crystal interfaces (Table 4), crucial because the interface is the boundary where breakdown processes occur (e.g. Slatt and Eyles, 1981; Cather and Folk, 1991; Palomares and Arribas, 1993; Caracciolo et al., 2012; Weltje et al., 2018). The amount of interfaces also correlates strongly with the environmental parameters (climate and topography) of the weathering efficiency (Heins, 1993, 1995).

3.4. X-ray diffraction (XRD)

X-ray diffraction (XRD) was used for qualitative and semi-quantitative mineralogical analyses of whole-rock (25 samples) (Table 5) and clay (<2 μm) fractions (16 samples) (Table 6). At the Department of Geosciences, University of Oslo, whole rock samples were micronised using a McCrone XRD-mill. The powder specimens were then prepared with the front-loading procedure and analysed by counting for 1.25 s at steps of 0.031°2θ from 2 to 65 °2θ, on a Bruker D8 Advance diffractometer with LynxEye 1-dimensional position sensitive detector (PSD), using Cu-Kα radiation (40 kV and 40 mA). Phase quantities were determined by Rietveld refinement (Rietveld, 1969) using PROFEX (v. 3.11.1) (Doebelin and Kleeberg, 2015). Clay samples were prepared by extracting the <2 μm fraction by gravity settling. Oriented aggregate mounts were prepared using the Millipore-filter transfer method (Moore and Reynolds, 1997) and analysed after four treatments: air-dried, treated with ethylene glycol vapour for 24 h, heated at 350 °C for 1 h, and heated at 550 °C for 1 h. The XRD data from the <2 μm fraction was recorded by counting for 0.3 s at steps of 0.01°2θ from 2 to 35 °2θ. The degree of interstratification and relative abundances of clay minerals were interpreted using NewMod II (v. 2.0) (Mertens et al., 2016).

The interpretation of clay minerals followed the procedures in Moore and Reynolds (1997). Peaks around 10 Å, that did not react to any treatments were identified as a mixture of illite and fine-grained mica (I + M) (Table 6, Fig. 12). Chlorite was identified by a basal series of diffraction peaks at 14.13 Å (001), 7.07 Å (002), 4.71 Å (003) and 3.53 Å (004) (Table 6, Fig. 12A). The last heat treatment of the sample (550 °C for 1 h) caused an increase in intensity of the 001 reflection, whereas the 002, 003 and 004 reflections experienced reduced intensities (Fig. 12A). The presence of smectite was suggested if peaks in the 14 Å region shifted to higher d-spacings after ethylene glycol treatment (Fig. 12A). Kaolinite was identified by peaks at around 7.16 Å and 3.58 Å that were destroyed by the last heat treatment (Fig. 12B). The kaolinite peaks were broad and asymmetric towards higher d-spacings, and could be decomposed into two partly overlapping reflections at around 7.14 Å and 7.35 Å, possibly indicating the presence of both an highly ordered and a poorly ordered kaolinite, or alternatively a dehydrated halloysite (Table 6, Fig. 12B) (Tan, 2014; Tan et al., 2017). Peaks in the 14 Å region that did not expand after glycolisation and subsequently collapsed to lower d-spacings after heat treatment, were compatible with vermiculite (Fig. 12B).

3.5. Whole rock geochemistry

Bulk chemical analyses of 17 samples by X-ray fluorescence (XRF) (Table 7) were carried out by Activation Laboratories Ltd. (Ontario, Canada), following analysis code WRA-XRF 4C (https://actlabs.com).

3.5.1. Mass balance calculation

The geochemical results (Table 7) were assessed following a geochemical mass balance approach (Brimhall and Dietrich, 1987; Driese et al., 2000; Braun et al., 2009) expressed by the open-system mass fraction transport function ($\tau_{j,w}$) (Eq. (1)). In mass balance calculations, one element is assumed immobile (subscript *i*) during weathering of the

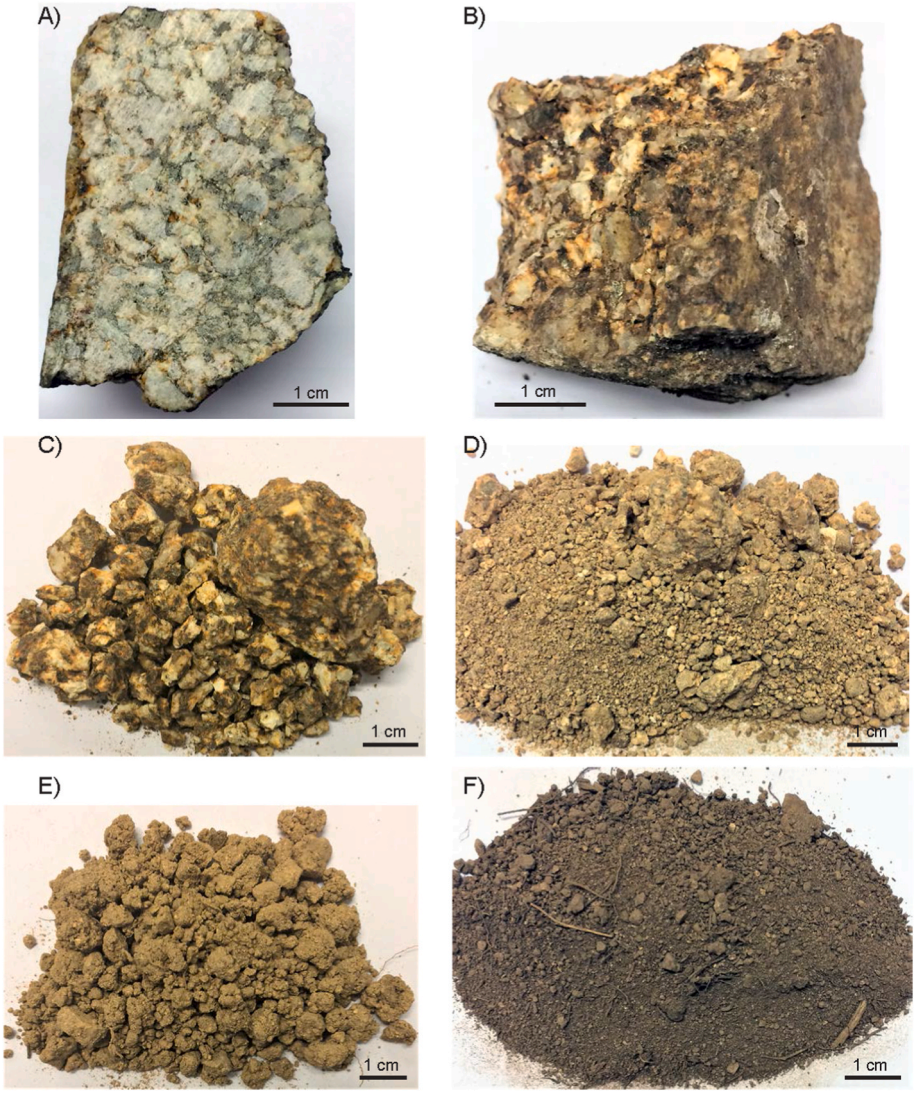

Fig. 3. Images of samples from the observed weathering facies and soil horizons with noted degree of weathering (W1 – W5). A) Sampled (3-20-17B) W2 material from altered coherent rock facies (ACR). B) Sampled (3-19-20B) W3 material from saprock facies. C) Sampled (3-4-17) W4 material from lower saprolite facies. D) Sampled (3-1-17B) W5 material from upper saprolite facies. E) Sampled (3-7-17) soil – Bw horizon. F) Sampled (3-1-17B) soil – A horizon.

parent material (subscript p), and thus making it possible to evaluate the losses and gains of mobile elements (subscript *j*) compared to the immobile element (subscript *i*) in the weathered samples (subscript w) (Sheldon and Tabor, 2009). In the present study, the least altered sample from the altered coherent rock facies (sample 3-20-17B) demonstrated similar mineralogical and chemical composition as fresh sample in Perri et al. (2015), and was thus assumed to be representative of the parent material in the area. Al_2O_3 was used as the immobile index element (Nesbitt and Young, 1982).

$$\tau_{j,w} = \frac{C_{j,w}C_{i,p}}{C_{j,p}C_{i,w}} - 1 \quad (1)$$

$\tau_{j,w}$ represents losses or gains of a mobile element in weathered sample, $C_{j,p}$ is the chemical concentration of a mobile element in weight percent (wt%) in parent material, $C_{j,w}$ is the chemical concentration (wt%) of a mobile element in weathered sample, $C_{j,p}$ and $C_{i,w}$ are the chemical concentrations (wt%) of immobile index element in parent and weathered material, respectively.

The bulk mass-transfer coefficient ($\tau_{b,w}$) (Hayes et al., 2019) (Eq. (2)), is the sum of all losses and gains of individual elements and represents the overall mass change during weathering of the parent material. $\tau_{b,w}$ is expressed by comparing the concentration of the immobile element (Al_2O_3) in the parent material ($C_{i,p}$) with the concentration of the immobile element in weathered materials ($C_{i,w}$) by:

$$\tau_{b,w} = \frac{C_{i,p}}{C_{i,w}} - 1 \quad (2)$$

3.5.2. Chemical index of alteration (CIA)

The chemical index of alteration (CIA) (Nesbitt and Young, 1982) estimates the chemical alteration of feldspar minerals and their hydration to clay minerals (Sheldon and Tabor, 2009), by measuring the fluxes of mobile base cations relative to Al_2O_3 using whole rock molar quantities and correcting for the presence of Ca-bearing phosphates (apatite) within the silicate fraction (McLennan, 1993).

$$CIA = \left(\frac{Al_2O_3}{Al_2O_3 + CaO^* + Na_2O}\right) \times 100 \quad (3)$$

$$CaO^* = CaO - \left(\frac{10}{3} \times P_2O_5\right) \quad (4)$$

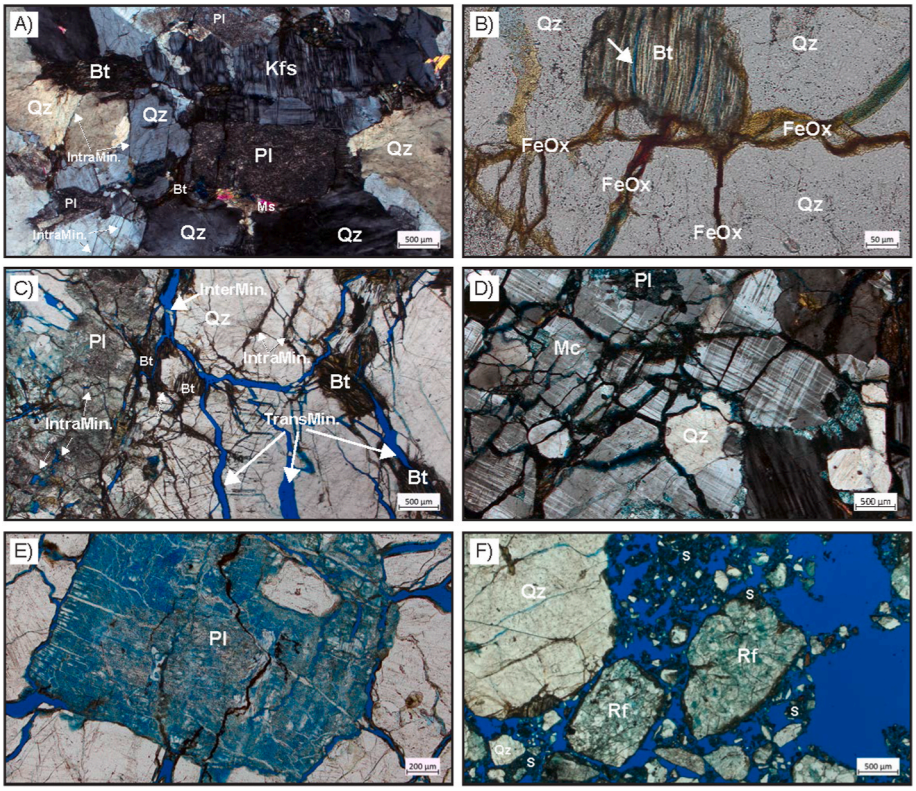

Fig. 4. Micrographs showing micromorphological features in different weathering facies. Pores highlighted by blue epoxy. A) Sampled (3-20-17B) altered coherent rock facies displaying fresh – nearly fresh pertithic K-feldspar, plagioclase, quartz, biotite and muscovite grains. Intramineral microfractures display small apertures and are predominantly closed. Note the severe sericitisation affecting plagioclase crystals (XPL). B) Sampled (3-19-17B) saprock facies showing opening of biotite (arrow), and the iron oxides in proximal microfractures. Note how the original brown colour of biotite in PPL is fading (PPL). C) Sampled (3-15-17B) lower saprolite facies showing an increase in frequency and aperture of transmineral microfractures compared to the ACR and saprock facies. Breakage of Pl/Qz crystal interface indicated by intermineral microfracture. Slight chemical alteration of plagioclase have resulted in the formation of intramineral dissolution pores partly filled by neoformed clays. Intramineral microfractures in quartz grain have been closed by dark brown material. Note the opening of altered biotite minerals following the original cleavage (PPL). D) Sampled (3-10-17B) upper saprolite facies. This is an example of increasing fracture aperture by dilation, causing fragmentation and grain-size reduction of a microcline grain. The result is an increase in rock volume. Note the chemical alteration of plagioclase inclusion and the absence of such in quartz inclusion (XPL). E) Sampled (3-3UD-17B) upper saprolite demonstrates strong alteration of a plagioclase grain. Note that the original polysynthetic twinning is still discernible (PPL). F) Sampled (3-2UD-17B) soil A horizon showing granitic rock fragments, quartz grains and brown soil particles (PPL). Abbreviations: PPL, plane polarised light; XPL, cross polarised light; Qz: quartz Pl, plagioclase; Kfs, K-feldspar; Mc, microcline, Bt: biotite; Ms, muscovite; FeOx, iron oxides; Rf, rock fragment, S, soil particles TransMin: transmineral pore, IntraMin.: intramineral pore, InterMin.: intermineral pore. (For interpretation of the references to colour in this figure legend, the reader is referred to the Web version of this article.)

3.5.3. Bulk density (ρ_b), calculated porosity (φ_c) and volumetric strain factor (ε)

Bulk densities (ρ_b) of undisturbed samples, collected by push corer, were estimated by measuring the dry weight of the sample while contained in the sample rings with known volume (100 cm^3) (Table 1). Bulk densities (ρ_b) of conventional samples from the altered coherent and saprock facies were determined by volume displacement.

Calculated porosities of weathered samples (φ_c) can be computed by assuming that changes in bulk densities (ρ_b) was the result of increasing porosity, whereas the grain density remained constant (Buss et al., 2017). The bulk density ($\rho_{b,p}$) of parent material (sample 3-20-17B) was taken as representative of the coherent rock grain density. The calculated porosity of a weathered sample ($\varphi_{c,w}$) can then be estimated by the ratio of bulk density of weathered material ($\rho_{b,w}$) with that of the parent material ($\rho_{b,p}$), by

$$\varphi_{c,w} = 100\left(1 - \frac{\rho_{b,w}}{\rho_{b,p}}\right) \quad (5)$$

The volumetric changes of weathered samples (ε) can be estimated by the relationship between the total mass loss (Eq. (2)) and the calculated porosity (Eq. (5)). The volumetric strain factor (ε), representing positive (dilational) or negative (collapse) volumetric change for a weathered sample, can thus be determined by the expression (Driese et al., 2000; Hayes et al., 2019):

$$\varepsilon_{i,w} = \left(\frac{\rho_{b,p}}{\rho_{b,w}} \times \frac{C_{i,p}}{C_{i,w}}\right) - 1 \quad (6)$$

3.5.4. Loss on ignition (LOI)

Loss on ignition (LOI) is routinely reported during XRF analysis and represents the weight loss after heating to 1050 °C. LOI has been applied successfully as an indicator of the degree of weathering (e.g. Regassa et al., 2014), as the amount of OH groups increase during weathering when anhydrous silicates are replaced by hydrous clay minerals (Velde and Meunier, 2008). In addition LOI is an approximation of the amount of organic matter and volatiles.

4. Results

4.1. Macromorphology

The altered coherent rock facies (ACR) (Figs. 2 and 3A) was recognised in outcrops by its minor red staining within and close to fractures. This indicates exposure to meteoric waters and oxidation of iron-bearing minerals, as the only prominent weathering feature. Otherwise, the ACR facies appears coherent and retains mechanical strength, and is categorised as W2–W3 on the degree of weathering scale.

In the overlying saprock facies (Fig. 3B) red staining is more pervasive, and the rock could easily be disaggregated with a hammer. The degree of weathering was estimated to be around W3–W4 (Figs. 2 and 3B). The lower saprolite facies (Fig. 3C) is a transitional stage between the coherent saprock and the incoherent upper saprolite (Fig. 3D).

Rock samples from the lower saprolite are strongly oxidised and could be broken apart by hand, and the degree of weathering is classified as W4–W5 (Figs. 2 and 3C). In the upper saprolite facies, the rock looses cohesion and could be dug out using only a spade, and degree of weathering is classified as W5 (Figs. 2 and 3D). A bleached horizon (Bw)

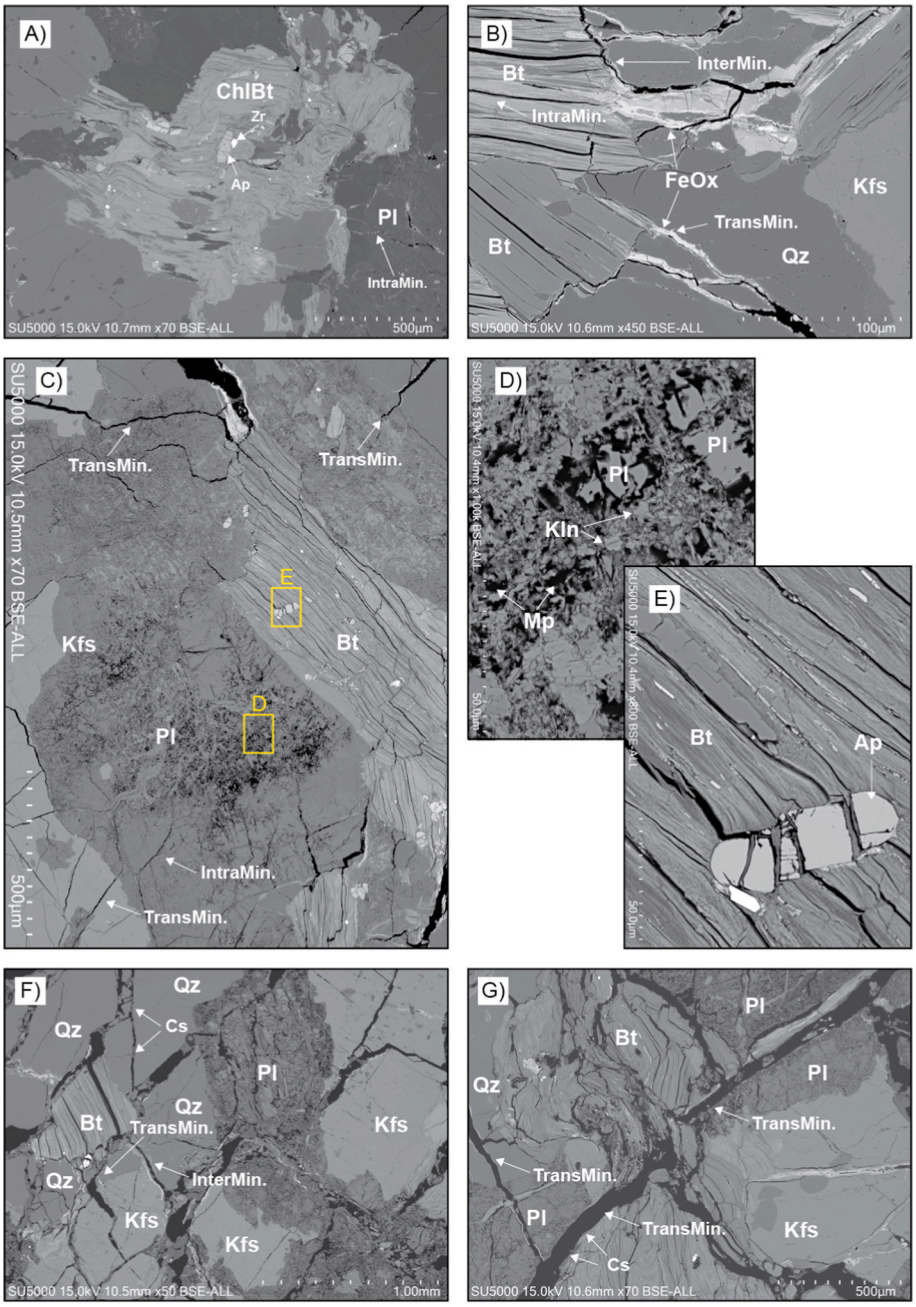

Fig. 5. SEM micrographs showing micromorphological alteration features in different weathering facies. A) Sampled (3-20-17B) altered coherent rock facies showing chloritised biotite (Chl = light grey, Bt = dark grey) with minute inclusions of e.g. apatite and zircon. Note the buckling and deformation of the mica grain. B) Sampled (3-19-17B) saprock facies showing the pseudomorphological transformation of biotite and opening of the mica along cleavage. Iron precipitated within microfractures near the host grain. C) Sampled (3-15-17B) lower saprolite facies shows the plagioclase weathering front. D) Close-up from C) shows detailed view of moderately altered plagioclase grain as mixture of microporosity, fine-grained material of original plagioclase, and neo-formed kaolinite. E) Close-up from C) showing the volumetric increase in altered biotite, demonstrated by the fragmented apatite inclusion. F, G) Samples (3-4UD-17B and 3-3UD-17B) from upper saprolite facies showing an increase in frequency and aperture of microfractures in advanced weathering stages. Grain contacts are broken by both interconnecting trans-mineral, and intermineral, fractures. Note the clay skins on the fracture walls. Abbreviations: Qz: quartz, Pl: plagioclase, Kfs: K-feldspar, Mc: microcline, Bt: biotite, Chl: chlorite Ms: muscovite, Kln: kaolinite, Mp: microporosity, FeOx: iron oxides, Rf: rock fragment, S: soil particles, Cs: clay skin. TransMin.: transmineral pore, IntraMin.: intramineral pore, InterMin.: intermineral pore.

(Figs. 2 and 3E) separates the upper saprolite from the upper dark brown, organic-rich soil A-horizon (Figs. 2 and 3F).

4.2. Micromorphology (petrography)

4.2.1. Weathering of individual grains

4.2.1.1. Biotite. In the altered coherent rock (ACR) and saprock facies, a majority of the observed biotite crystals had previously experienced partial-to-complete metasomatic chloritisation, as reflected in change of colour from shades of brown to pale green, under microscopic inspection in plane polarised light (PPL) (Fig. 4A and B). Additionally, the biotite crystals are speckled with minute inclusions of apatite, zircon and Ti-oxides, as identified in SEM (Fig. 5A).

It was estimated that about half of the observed biotite grains in the ACR facies had undergone 2–25% pseudomorphological transformation from brown and green to pale and white colours in PPL, whereas less than one third had experienced a transformation of 25–75% (Fig. 6). About 20% of the biotite grains were identified as fresh or nearly fresh. Liberation of structural Fe from slightly deformed biotite crystals resulted in the original mica grains acquiring a discoloured or bleached appearance (Fig. 4A and B). The low mobility of Fe is demonstrated by the precipitation of Fe-oxide-hydroxides in close proximity of the source mineral, i.e. between exfoliated biotite lamellae, in microfractures that had extended to neighbouring crystals subparallel to the mica cleavage, or as staining on adjacent mineral surfaces (Figs. 4B and 5B). In the saprock facies, more than three-quarters of the biotite grains are categorised as slightly altered (Fig. 6).

In the lower saprolite facies, there is a notable increase in the degree of biotite alteration. More than half the biotite grains are grouped as moderately altered, i.e. 25–75% of the viewed original grain is pseudomorphically transformed to a new mineralogical phase (Figs. 4C and

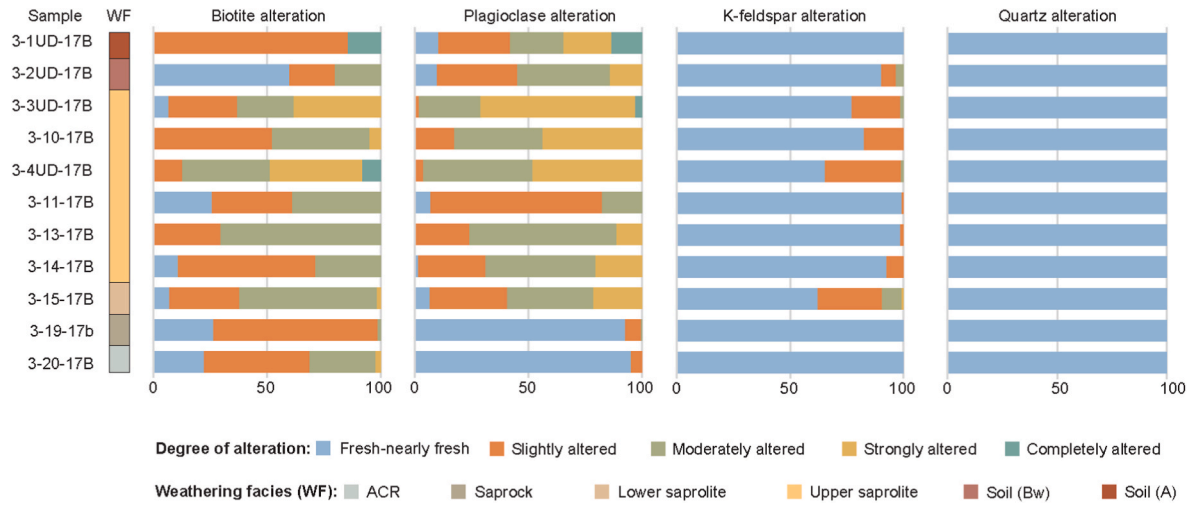

Fig. 6. Alteration of most common minerals up through the weathering profile, following classification by Stoops et al. (1979): Fresh-nearly fresh (<2.5% transformed to secondary material), slightly altered (2.5–25% transformed to secondary material), moderately altered (25–75% transformed to secondary material), strongly altered (75–97.5% transformed to secondary material), and completely altered (>97.5% transformed to secondary material).

Table 3
Key to point counting of interface types.

Abbreviation	Full name	Interface type
Qz/Qz	Quartz/Quartz	Isomineralic
Kfs/Kfs	K-feldspar/K-feldspar	Isomineralic
Pl/Pl	Plagioclase/Plagioclase	Isomineralic
Qz/Kfs	Quartz/K-feldspar	Anisomineralic - Isostructural
Qz/Pl	Quartz/Plagioclase	Anisomineralic - Isostructural
Qz/Bt	Quartz/Biotite	Anisomineralic – Anisostructural
Qz/Ms	Quartz/Muscovite	Anisomineralic – Anisostructural
Qz/Chl	Quartz/Chlorite	Anisomineralic – Anisostructural
Qz/Opq	Quartz/Opaque	Anisomineralic – Anisostructural
Qz/Ttn	Quartz/Titanite	Anisomineralic – Anisostructural
Pl/Kfs	Plagioclase/K-feldspar	Anisomineralic - Isostructural
Pl/Bt	Plagioclase/Biotite	Anisomineralic – Anisostructural
Pl/Ms	Plagioclase/Muscovite	Anisomineralic – Anisostructural
Pl/Zrn	Plagioclase/Zircon	Anisomineralic – Anisostructural
Pl/Chl	Plagioclase/Chlorite	Anisomineralic – Anisostructural
Pl/Ep	Plagioclase/Epidote	Anisomineralic – Anisostructural
Kfs/Bt	K-feldspar/Biotite	Anisomineralic – Anisostructural
Kfs/Ms	K-feldspar/Biotite	Anisomineralic – Anisostructural
Bt/Bt	Biotite/Biotite	Isomineralic
Bt/Opq	Biotite/Opaque	Anisomineralic – Anisostructural
Bt/Ms	Biotite/Muscovite	Anisomineralic - Isostructural
Bt/Zrn	Biotite/Zircon	Anisomineralic – Anisostructural
Kfs/Opq	K-feldspar/Opaque	Anisomineralic – Anisostructural
Pl/Opq	Plagioclase/Opaque	Anisomineralic – Anisostructural
Bt/Chl	Biotite/Chlorite	Anisomineralic - Isostructural
Ms/Zrn	Muscovite/Zircon	Anisomineralic – Anisostructural
Ms/Ms	Muscovite/Muscovite	Isomineralic
Ms/Opq	Muscovite/Opaque	Anisomineralic – Anisostructural

Note: Interface types described using combination of the letters defined above. For example, Qz/Qz represents an isomineralic interface between quartz and quartz, Pl/Pl represents an isomineralic interface between plagioclase and plagioclase; Qz/Opq represents an anisostructural interface between quartz and an opaque mineral.

5C). Morphologically, most biotite grains at this level display deformation such as curling, buckling and expansion perpendicular to the c-axis (Figs. 4C and 5C, E).

The progressive pseudomorphic transformation of biotite increases upwards in the saprolite facies, culminating in the uppermost saprolite sample where >30% of the biotite grains are labelled as strongly altered, i.e. 75–97.5% of the original grain is transformed into a new mineral phase and only occasional grains remain unaltered (Fig. 6).

In the soil samples, only a few altered biotite grains were observed in the B-horizon, with more than half of the grains categorised as fresh – nearly fresh, and around 80% are classified as slightly altered in the A-horizon (Fig. 6).

4.2.1.2. Plagioclase. In the ACR and saprock facies, >95% of the observed plagioclase grains are categorised as fresh – nearly fresh (Fig. 6). However, the typical optical features of fresh plagioclase, such as polysynthetic twinning, are obscured by numerous minute inclusions of metasomatic sericite (Fig. 4A). In a few plagioclase grains an irregular speckled pattern of transformation has taken place along intramineral microfractures. Isolated intramineral pores are either open or occupied by clays with Mg-rich chemical composition that also include subordinate K and Ca, as revealed by their EDS spectra. Slight alteration has taken place along open transmineral microfractures that transect plagioclase grains, represented by neoformed material growing on the fracture wall. In addition, a dark brown material, identified as Fe-oxide-hydroxide by the EDS spectra, was observed, either as precipitates within transecting microfractures or along cleavage planes.

Intensification of plagioclase alteration was observed in samples from the lower saprolite facies, where >30% of the grains are categorised as slightly altered, >30% as moderately altered and >20% as strongly altered (Fig. 6).

Plagioclase alteration appears to increase upwards in the saprolite interval with the exception of one sample (3-11-17B) (Fig. 6). The plagioclase crystals are pseudomorphically replaced by secondary material (clays) where the original crystal outline is preserved and even original polysyntethic lamellae are vaguely visible, suggesting preferential replacement (Fig. 4E). In the uppermost saprolite sample, close to 70% of the observed plagioclase grains are categorised as strongly altered, i.e. between 75 and 97.5% of the grain replaced by clays, mainly kaolinite, as identified by booklet morphology in SEM and by the EDS spectra (Fig. 6).

As for the biotite, there is much greater variation in the degree of alteration displayed by grains in the soil samples, ranging from fresh – nearly fresh to completely altered, with the majority of grains being classified as slightly to moderately altered (Figs. 5F and 6).

4.2.1.3. K-feldspar (microcline and perthithic feldspar). Visible signs of chemical alteration of K-feldspar were not observed in the ACR and saprock facies (Fig. 4A). In the saprolite facies, minor alteration ha s taken place along the fracture walls of transmineral microfractures. Upwards in the saprolite facies, with increasing influence of microfracturing, K-feldspar grains are broken into smaller angular fragments (Fig. 4D), but still relatively unaffected by chemical alteration (Fig. 6).

Table 4
Results from point-counting of interface types.

Sample	3-1UD-17B	3-8-17	3-2UD-17B	3-7-17	3-3UD-17B	3-4UD-17B	3-6-17	3-5-17	3-4-17	3-3-17	3-2-17
Facies	Soil (A)	Soil (A)	Soil (Bw)	Soil (Bw)<	Sapr (U)	Sapr (U)	Sapr (L)	Sapr (L)	Sapr (L)	Sapr (L)	ACR
N	N = 174	N = 148	N = 179	N = 357	N = 167	N = 288	N = 500	N = 478	N = 500	N = 500	N = 500
Qz/Qz	29.9	33.8	23.5	12.3	17.4	26.0	7.8	14.6	11.0	22.6	20.8
Kfs/Kfs	2.3	0.7	1.7	2.8	2.4	2.1	1.0	1.7	2.8	1.8	5.0
Pl/Pl	2.9	8.8	2.2	4.2	0.6	0.7	3.6	3.3	4.4	7.2	4.4
Bt/Bt	0.0	0.0	0.0	0.0	0.0	0.0	0.8	0.8	0.0	0.0	0.0
Ms/Ms	0.0	0.0	0.0	0.0	0.0	0.0	0.0	0.4	0.0	0.0	0.0
Qz/Kfs	9.8	0.7	6.7	7.6	9.6	11.5	4.8	6.3	9.6	3.4	12.4
Qz/Pl	15.5	18.2	23.5	10.1	19.8	22.9	3.4	14.4	1.6	17.8	10.4
Pl/Kfs	14.4	3.4	9.5	6.2	19.8	13.5	25.6	7.9	16.6	9.0	13.6
Qz/Bt	6.3	6.1	7.3	13.4	7.8	8.7	4.6	16.3	1.2	1.8	10.2
Pl/Bt	0.6	4.7	3.4	18.8	1.8	3.8	1.6	9.8	4.2	4.4	6.0
Kfs/Bt	5.2	1.4	6.7	12.9	4.2	4.5	21.6	12.6	16.8	2.0	3.8
Bt/Ms	1.1	0.0	0.0	0.6	0.6	1.0	3.0	1.0	3.2	0.0	1.6
Pl/Ms	1.1	0.7	0.0	1.4	1.8	2.4	1.4	4.0	1.2	0.8	2.2
Kfs/Ms	0.0	0.7	0.6	1.7	0.0	0.0	3.4	1.7	1.2	0.2	1.0
Qz/Ms	0.6	0.7	2.8	0.8	2.4	1.0	0.2	0.2	0.0	0.2	3.0
Bt/Opq	8.0	2.7	8.4	3.1	7.8	0.3	8.4	1.5	11.4	4.4	1.6
Kfs/Opq	0.6	3.4	0.6	2.8	2.4	0.7	3.8	0.8	8.8	7.4	0.6
Pl/Opq	0.6	2.0	0.0	0.0	0.0	0.3	0.2	0.6	2.6	7.4	0.4
Qz/Opq	0.6	9.5	3.4	0.0	1.2	0.3	0.4	0.0	2.8	6.4	0.8
Ms/Opq	0.0	0.7	0.0	0.0	0.0	0.0	0.0	0.0	0.0	0.0	0.0
Bt/Chl	0.0	0.0	0.0	0.0	0.0	0.0	3.2	0.2	0.0	0.0	1.8
Qz/Chl	0.0	2.0	0.0	0.3	0.6	0.0	0.0	0.0	0.0	0.0	0.0
Pl/Chl	0.0	0.0	0.0	1.1	0.0	0.0	0.4	0.0	0.4	0.0	0.0
Pl/Zrn	0.0	0.0	0.0	0.0	0.0	0.0	0.0	1.7	0.2	0.2	0.0
Bt/Zrn	0.6	0.0	0.0	0.0	0.0	0.0	0.6	0.0	0.0	0.0	0.0
Ms/Zrn	0.0	0.0	0.0	0.0	0.0	0.0	0.0	0.0	0.0	0.0	0.0
Grt/Bt	0.0	0.0	0.0	0.0	0.0	0.0	0.0	0.0	0.0	0.0	0.2
Grt/Qz	0.0	0.0	0.0	0.0	0.0	0.0	0.0	0.0	0.0	0.0	0.2
Pl/Ep	0.0	0.0	0.0	0.0	0.0	0.0	0.0	0.0	0.0	0.0	0.0
Qz/Ep	0.0	0.0	0.0	0.0	0.0	0.0	0.0	0.0	0.0	0.8	0.0
Kfs/Ep	0.0	0.0	0.0	0.0	0.0	0.0	0.0	0.0	0.0	0.2	0.0
Pl/Ep	0.0	0.0	0.0	0.0	0.0	0.0	0.2	0.0	0.0	0.8	0.0
Kfs/Ser	0.0	0.0	0.0	0.0	0.0	0.0	0.0	0.0	0.0	1.2	0.0
Total	100.0	100.0	100.0	100.0	100.0	100.0	100.0	100.0	100.0	100.0	100.0

Note: the reported results represent % of interface types of the total number of counted interfaces (N) for each sample.
Explanation of abbreviations.
Facies: Sapr (U): upper saprolite facies, Sapr (L): lower saprolite facies, ACR: altered coherent rock facies.

During fragmentation of the grains, displacement mainly occurs by dilation, i.e. in the direction perpendicular to the fracture wall. Plagioclase inclusions within the microcline crystals are affected by alteration, albeit to a lesser degree than the individual plagioclase crystals in the sample.

4.2.1.4. Quartz. Quartz was observed to be chemically unaltered, but the grains are transected by a few, short, closely spaced hair-like microfractures in the ACR facies, features that increase in frequency and aperture upwards (Fig. 4). In the advanced weathering stages, the original quartz grains are fragmented into smaller angular fragments, with displacement mainly occurring perpendicular to the fracture walls (dilation) (Fig. 4C, D, F).

4.2.2. Porosity

4.2.2.1. Altered coherent rock facies. Observed pores (φ_{obs}) make up <5% of the total area analysed in thin sections from the ACR facies, and include all three fracture categories (Figs. 7 and 8), the majority being categorised as closed fractures (Fig. 7). Microfractures were observed to traverse multiple grains, both as open pores or closed by Mg- and Fe-rich clays with a chemical composition revealed by EDS spectra (Figs. 4B and 5B). In some cases, transmineral pores were observed radiating from the tip of exfoliated biotite grains (Fig. 5B); they are completely or partially infilled by dark brown material, with an EDS spectra indicating a material enriched with Fe or Ti. Isolated pores are present as intramineral microfractures that follow the cleavage planes in feldspars (Fig. 9A and B). Slight weathering had taken place along intramineral pores in plagioclase, and these are partly open or filled by clays with a composition including Mg, Fe and K (Fig. 9A). The few intermineral fractures at grain contacts are principally observed in connection with slightly altered plagioclase and biotite grains, being infilled by neoformed clays or Fe-oxide-hydroxide and Ti-oxides.

4.2.2.2. Saprock facies. Samples from the saprock facies display an increase in φ_{obs}, compared to the ACR facies (Fig. 7), where the φ_{obs} at this level accounted for 7% of the bulk rock. In contrast to the ACR facies, the majority of pores are open (Fig. 7). More than 60% of the φ_{obs} are interconnected microfractures transecting multiple grains that are also joined by open intermineral pores (Fig. 9B). The majority of fractures are classified as open or partially open, with fracture walls covered by a thin veneer of clays (Figs. 4B, 5B and 9C, D). Microfractures that transect plagioclase are partially to completely occluded by clays.

4.2.2.3. Lower saprolite facies. Through the transition to saprolite facies, φ_{obs} almost doubles compared to the saprock facies, and make up about 12% of the total rock (Fig. 7). Compared to the saprock samples, microfractures in the lower saprolite facies are more frequent and display enlarged apertures (Fig. 9E). A combination of different types of pores make up a dense network of interconnected microfractures that in some instances result in the breaking up of quartz and feldspar grains into smaller, angular fragments that have not experienced any notable

Table 5
Semi-quantitative mineralogical results in PROFEX of selected XRD whole-rock samples. .

Sample	Facies	Qz	Kfsp	Pl	M + I	Chl	Kln	Vrm	Total
3-1-17b	Soil (A)	40	26	19	4	2	7	1	100
3-8-17	Soil (A)	43	26	19	3	2	7	1	100
3-2-17b	Soil (A)	40	27	20	4	2	7	1	100
3-3-17b	Soil (A)	42	23	21	4	4	5	1	100
3-4-17b	Soil (A)	39	26	20	4	3	7	1	100
3-5-17b	Soil (A)	40	26	19	3	4	7	1	100
3-6-17b	Soil (A)	41	22	22	5	2	7	1	100
3-7-17b	Soil (Bw)	42	27	20	4	2	5	1	100
3-7-17	Soil (Bw)	43	28	16	4	3	5	1	100
3-8-17b	Saprolite (U)	37	35	14	3	2	6	1	100
3-9-17b	Saprolite (U)	40	37	12	3	2	5	1	100
3-10-17b	Saprolite (U)	40	35	15	3	2	5	1	100
3-11-17b	Saprolite (U)	37	37	17	2	2	4	1	100
3-12-17b	Saprolite (U)	34	39	13	3	2	6	2	100
3-13-17b	Saprolite (U)	38	33	16	5	3	5	1	100
3-14-17b	Saprolite (U)	39	37	14	3	2	4	1	100
3-6-17	Saprolite (L)	36	34	25	4	1	0	0	100
3-5-17	Saprolite (L)	37	30	23	4	1	5	0	100
3-15-17b	Saprolite (L)	25	47	17	6	0	5	1	100
3-4-17	Saprolite (L)	29	43	21	6	0	0	0	100
3-3-17	Saprolite (L)	30	46	21	3	0	0	0	100
3-19-17b	Saprock	12	60	18	4	5	0	0	100
3-2-17	ACR	44	35	16	6	0	0	0	100
3-20-17b	ACR	37	20	27	5	11	0	0	100

Explanation of abbreviations in.
Facies: Soil (A): Soil A-horizon, Soil (Bw): soil Bw-horizon, Saprolite (U): upper saprolite facies, Saprolite (L): lower saprolite, Saprock: saprock facies, ACR: altered coherent rock facies.
Minerals: Qz: quartz, Kfsp: K-feldspar, Pl: plagioclase, M + I: mica and illite, Chl: chlorite, Kln: kaolinite, Vrm: vermiculite.

Table 6
Semi-quantitative analysis in NewMod of selected XRD clay samples (<2 μm).

Sample	Facies	I + M	Vrm	Kln (ord.)[a]	Kln (disord.)[b]	Chl-Sm	Chl	Total
3-1-17B	Soil (A)	29	12	59	0	0	0	100
3-2-17B	Soil (A)	25	21	54	0	0	0	100
3-3-17B	Soil (A)	26	12	62	0	0	0	100
3-4-17B	Soil (A)	23	16	61	0	0	0	100
3-5-17B	Soil (A)	21	11	68	0	0	0	100
3-7-17B	Soil (Bw)	13	7	47	33	0	0	100
3-8-17B	Saprolite (U)	17	5	41	37	0	0	100
3-9-17B	Saprolite (U)	15	6	21	58	0	0	100
3-10-17B	Saprolite (U)	16	5	47	32	0	0	100
3-11-17B	Saprolite (U)	17	3	7	73	0	0	100
3-12-17B	Saprolite (U)	14	7	31	48	0	0	100
3-13-17B	Saprolite (U)	14	4	29	53	0	0	100
3-14-17B	Saprolite (U)	16	6	29	49	0	0	100
3-15-17B	Saprolite (L)	22	6	0	4	68	0	100
3-19-17B	Saprock	17	0	0	0	72	11	100
3-20-17B	ACR	25	0	0	0	35	40	100

Facies: Soil (A): Soil A-horizon, Soil (Bw): soil Bw-horizon, Saprolite (U): upper saprolite facies, Saprolite (L): lower saprolite, Saprock: saprock facies, ACR: altered coherent rock facies.
Clay minerals: I + M: illite and fine-grained mica, Vrm: vermiculite, Kln (ord.): well-crystalline kaolinite, Kln (disord.): poorly crystalline kaolinite, Chl-Sm: mixed-layered chlorite-smectite, Chl: chlorite.
Explanation of abbreviations in.
Notes: results represent % of each clay phase summed to 100.
[a] Highly-ordered kaolinite identified with peaks around 7.14 Å.
[b] Poorly-ordered kaolinite identified with peaks around 7.35 Å.

chemical alteration (Figs. 5C and 9E, F). Several examples of opening of multiple wafers in a single biotite grain were observed (Figs. 4C and 5C, D). The microfractures with the largest apertures are open, but coated by a film of dark brown, Fe-rich material on the fracture walls. The microfractures with smaller apertures are generally open, except within the altered plagioclase grains, where most pores are infilled by clays (Fig. 9E and F).

4.2.2.4. Upper saprolite facies. With increasing alteration of plagioclase grains in the saprolite facies, intramineral pores were more frequently observed (Figs. 8 and 9G, H). In SEM, the intramineral pores were observed to be either open or filled by kaolinite clays, identified by the booklet morphology and EDS spectra. The breakage of single feldspar and quartz grains combined with an increase in open intermineral fractures and intramineral pores in plagioclase, reduce the grain size of the saprolite compared to the ACR and saprock weathering facies. In the saprolite texture, individual crystals or crystal fragments are separated by a network of either open and coated or partly infilled interconnected pores (Fig. 9G and H).

In an undisturbed sample (3-4UD-17B) from 90 cm below the reference level, microlaminated clay coatings with crescent morphology were observed as infillings. At this level, intramineral pores in strongly

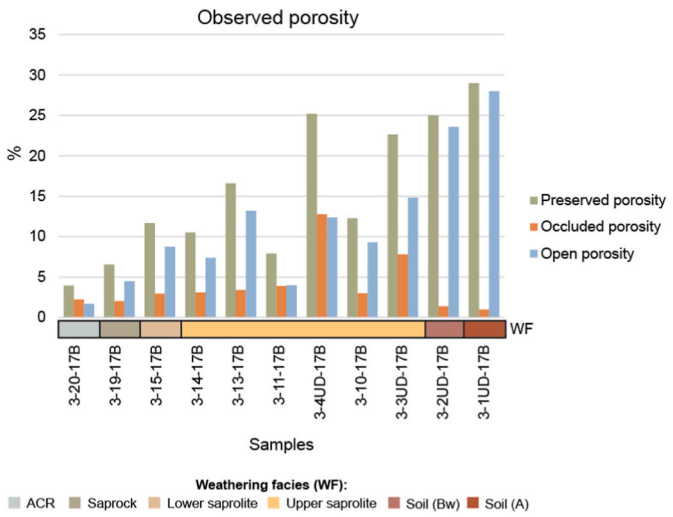

Fig. 7. Observed porosity in thin sections. A) total porosity, B) occluded porosity, (C) preserved porosity (see Table 2).

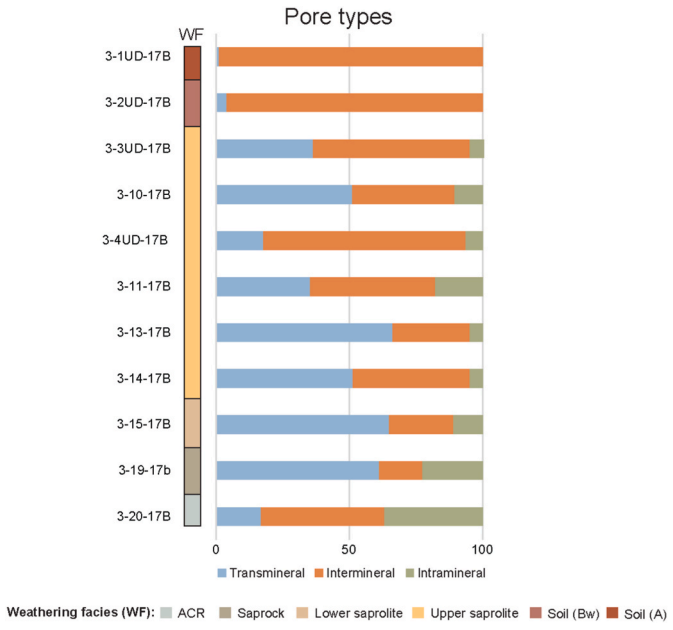

Fig. 8. Percentages of pore types observed in thin sections (see Table 2). Intramineral: within a mineral grain, transmineral: traverse within the rock, not following grains boundaries, and intermineral: traverse within the rock but following grain contacts.

altered plagioclase grains are the dominating pore type. The intermineral space is partly infilled by mixed material made up of fine-grained angular fragments of primary minerals and soil aggregates floating in a matrix of kaolinite (Fig. 5F). The intermineral mixed material is cut by channels coated by material that were deposited parallel to the fracture wall. In the uppermost saprolite sample (3-3UD-17B), total pores that were distinguishable under the microscope make up about 25% of the thin section, and more than half of these pores are classified as open. The texture is similar to that in 3-4UD-17B, but with increased number and width of fractures and increased portion of intramineral pores, all as a result of plagioclase weathering (Figs. 4E and 5F, G and 9G, H). The original rock texture is still essentially reproducible, since the disaggregated grains are mainly transposed perpendicular to the fracture walls without rotation or significant displacive movement parallel to the fracture.

4.2.2.5. Soil. The samples from the soil horizons consist of a mixture of rock fragments, single mineral grains, soil aggregates and organic material, separated by intermineral pores. The original rock texture is no longer preserved. Rock fragments display variable degree of weathering, including plagioclase grains ranging in weathering degree from fresh–nearly fresh to strongly altered. The rock fragments are subangular, and grooves on the surface of the fragments are coated by dark brown soil material (Fig. 4F). When moving from the Bw to the A soil horizon there is a reduction in the rock clast to soil aggregate ratio, and a slight increase in intermineral pores (Fig. 8).

4.2.3. Crystal interfaces

The proportion of overall interfaces is evenly distributed in the altered coherent rock and lower saprolite facies. The reduction of total interfaces observed in the more advanced weathering stages, i.e. from upper saprolite facies and upwards, indicates splitting of previously interlocking interfaces.

4.2.3.1. Isomineralic interfaces. Five isomineralic interface types were identified. Their relative mechanical durability, from most to least durable, can be summarised as follows: Qz/Qz > Kfs/Kfs > Pl/Pl > Bt/Bt > Ms/Ms (Table 4, Fig. 10A, B, C). Isomineralic interfaces involving a phyllosilicate crystal, such as biotite/biotite (Bt/Bt interface) and muscovite/muscovite (Ms/Ms interface), are very few, representing <1% of the counted interfaces (Table 4).

4.2.3.2. Anisomineralic isostructural interfaces. By comparing Qz/Pl, Pl/Kfs and Qz/Kfs interfaces, the boundary between plagioclase and quartz (Qz/Pl) appears to be more durable than the boundary between the plagioclase and adjacent alkali feldspars (Pl/Kfs), whereas Qz/Kfs interfaces are the least durable (Fig. 10D, E, F). Mixed tectosilicate interfaces, such as Qz/Pl, Pl/Kfs and Qz/Kfs, are more durable than anisomineralic isostructural interfaces between phyllosilicates such as Bt/Ms and Bt/Chl (Table 4). A few inclusions of accessory minerals, such as zircon within plagioclase or muscovite, and epidote within plagioclase were counted as interfaces (Table 4).

4.2.3.3. Anisomineralic interfaces involving phyllosilicates. In the Sila grus samples it appeared that the durability of biotite is higher when it adjoined a quartz crystal than plagioclase, whereas the Kfs/Bt contact displays a more ambiguous trend that was difficult to interpret (Fig. 10G, H, I). Other anisostructural interfaces involving phyllosilicates are muscovite-rich, such as Qz/Ms, Pl/Ms, Kfs/Ms (Table 4). Qz/Ms interfaces occurred in trace amounts in three arenaceous saprolite horizon depths and are lacking in the deepest; Pl/Ms interfaces are more numerous in the upper saprolite interval (4%) and decrease to 0.4% in the deepest one; Kfs/Ms interfaces have the same value in the first two summit saprolite horizons but are absent from the deepest (Table 4). Interfaces between chlorite and a tectosilicate such as Qz/Chl and Pl/Chl occur only in trace amounts and are lacking in the upper arenaceous saprolite horizons.

4.3. X-ray diffraction (XRD)

4.3.1. Whole rock XRD

Two-mica, medium-grained monzogranite-granodiorite characterises the Sila granite composition at this locality. The main constituents in the ACR facies are quartz, plagioclase and K-feldspar (Table 5). Chloritised biotite dominates over muscovite in the mica association. The Pl/(Pl + Qz) ratio (Table 5, Fig. 11) is used as an indicator of chemical weathering, and shows that one sample from the saprock facies actually displays a higher ratio than the ACR facies, possibly reflecting variations in the primary composition, rather than alteration (Fig. 11). Compared to the saprock, the Pl/(Pl + Qz) ratio decreases markedly in the lower saprolite facies, and is further reduced in the upper saprolite facies

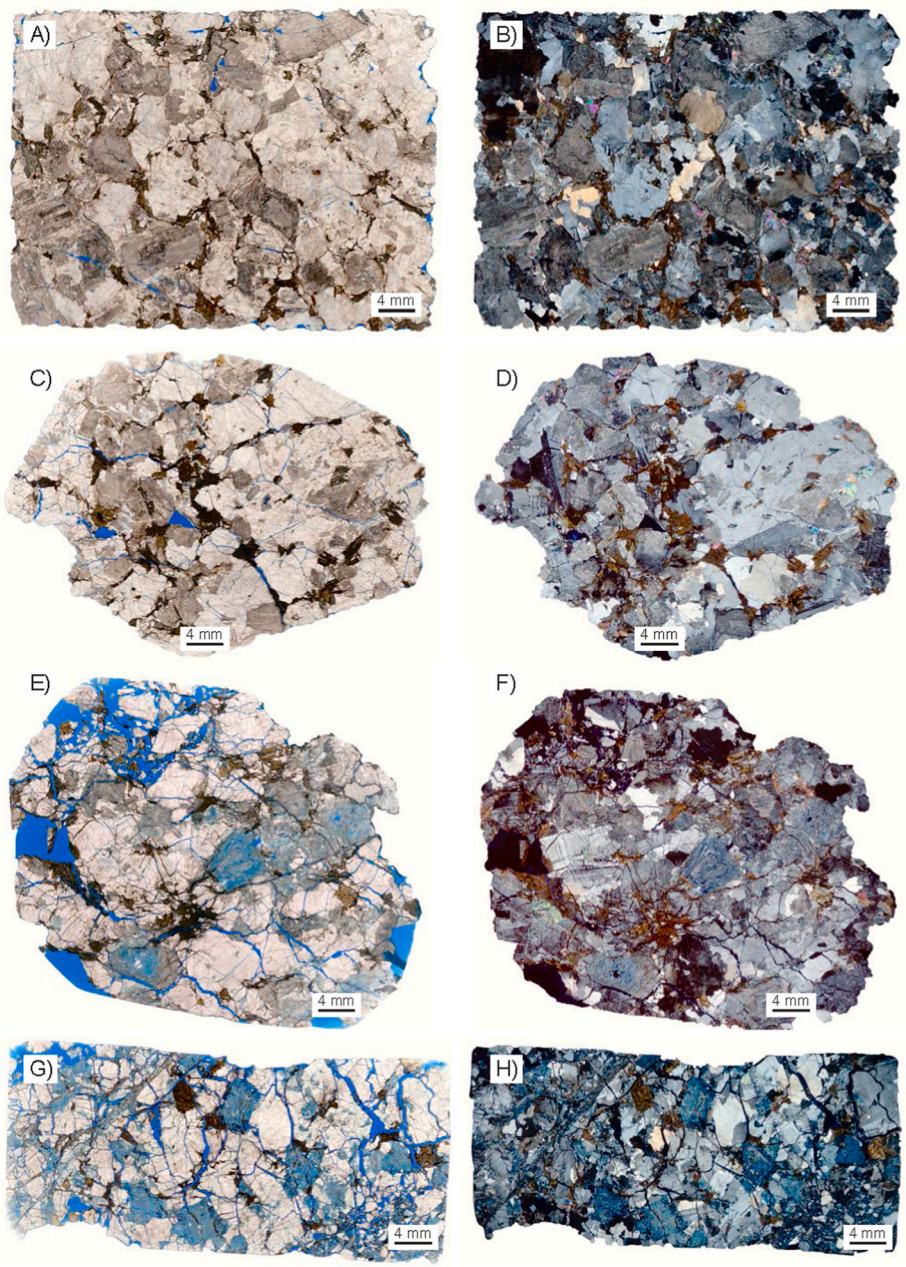

Fig. 9. Paired (PPL and XPL) thin sections scans showing the micromorphological development of the weathering facies up through the regolith profile. Pores highlighted by blue epoxy (see Table 2). A) (PPL), B) (XPL) Sampled (3-20-17B) altered coherent rock facies showing closely interlocking crystals, with only a few microfractures visible at the scale of the thin section. C) (PPL), D) (XPL) Sampled (3-19-17B) saprock facies showing increase in microfracture frequency. E) (PPL), F) (XPL) Sampled (3-15-17B) lower saprolite facies representing the plagioclase weathering front. Minor formation of intermineral porosity within slightly, moderately and strongly altered plagioclase grains. Trans- and intermineral microfractures have increased in frequency and aperture compared to less altered weathering facies. G) (PPL), H) (XPL) Sampled (3-3UD-17B) upper saprolite facies showing intramineral porosity developing within moderately to strongly altered plagioclase grains. Trans- and intermineral microfractures dominate the pore space, and have increased in frequency and aperture compared to the lower saprolite facies. . (For interpretation of the references to colour in this figure legend, the reader is referred to the Web version of this article.)

(Table 5, Fig. 11). However, a slight increase in the Pl/(Pl + Qz) ratio was observed in the soil horizons, compared to the underlying saprolite.

Chlorite is the dominant clay-sized mineral in the ACR and saprock facies, and appears both as inherited, fine-grained micaous grains and as neoformed clays. The first appearance of kaolinite and vermiculite in whole rock samples was observed in the lower saprolite facies (Table 5, Fig. 11), but the total clay content never exceeds 10% of the total rock throughout the profile.

4.3.2. *Clay mineralogy XRD (<2 μm)*

In sample from the ACR facies (3-20-17B), chlorite is the most abundant mineral, making up around 40% of the clay fraction, (Table 6, Fig. 12A). The dominant chlorite peaks at ~14 Å and ~7 Å partly obscure an overlapping mineral phase in air dried state that shifts to higher d-spacings after glycolisation, to 16.9 Å and 7.6 Å respectively (Fig. 12A). Peak positions for the expanding phase are not consistent with pure smectite, but is interpreted to represent a mixed-layered mineral, possibly chlorite-smectite (35%) (Table 6, Fig. 12A). Illite and/or fine-grained mica (I + M) (25%) are represented by a reflection at 9.93 Å (Table 6, Fig. 12C).

In the saprock facies (sample 3-19-17B), the mixed-layered expanding phase (chlorite-smectite) is dominating (73%) over I + M (17%) and chlorite (11%), in the clay fraction (Table 6, Fig. 12C).

The sample that represents the transition from saprock to saprolite facies (3-15-17B) contains the first traces of kaolinite (4%). The clay fraction of the sample, however, is dominated by chlorite-smectite (68%) with subordinate I + M (22%), and vermiculite (6%) (Table 6, Fig. 12C).

The clay fraction of the seven saprolite samples are dominated by kaolinite (~80%), with accessory I + M (15%) and vermiculite (~5%) (Table 6, Fig. 12B and C). There are no obvious changes in the distribution of the individual clays upwards in the saprolite facies, however the highly ordered kaolinite polytype appears to increase stratigraphically upwards at the expense of poorly ordered polytype.

Clay mineralogy from the Bw soil horizon is similar to the underlying saprolite, being kaolinite dominated, with minor I + M and vermiculite

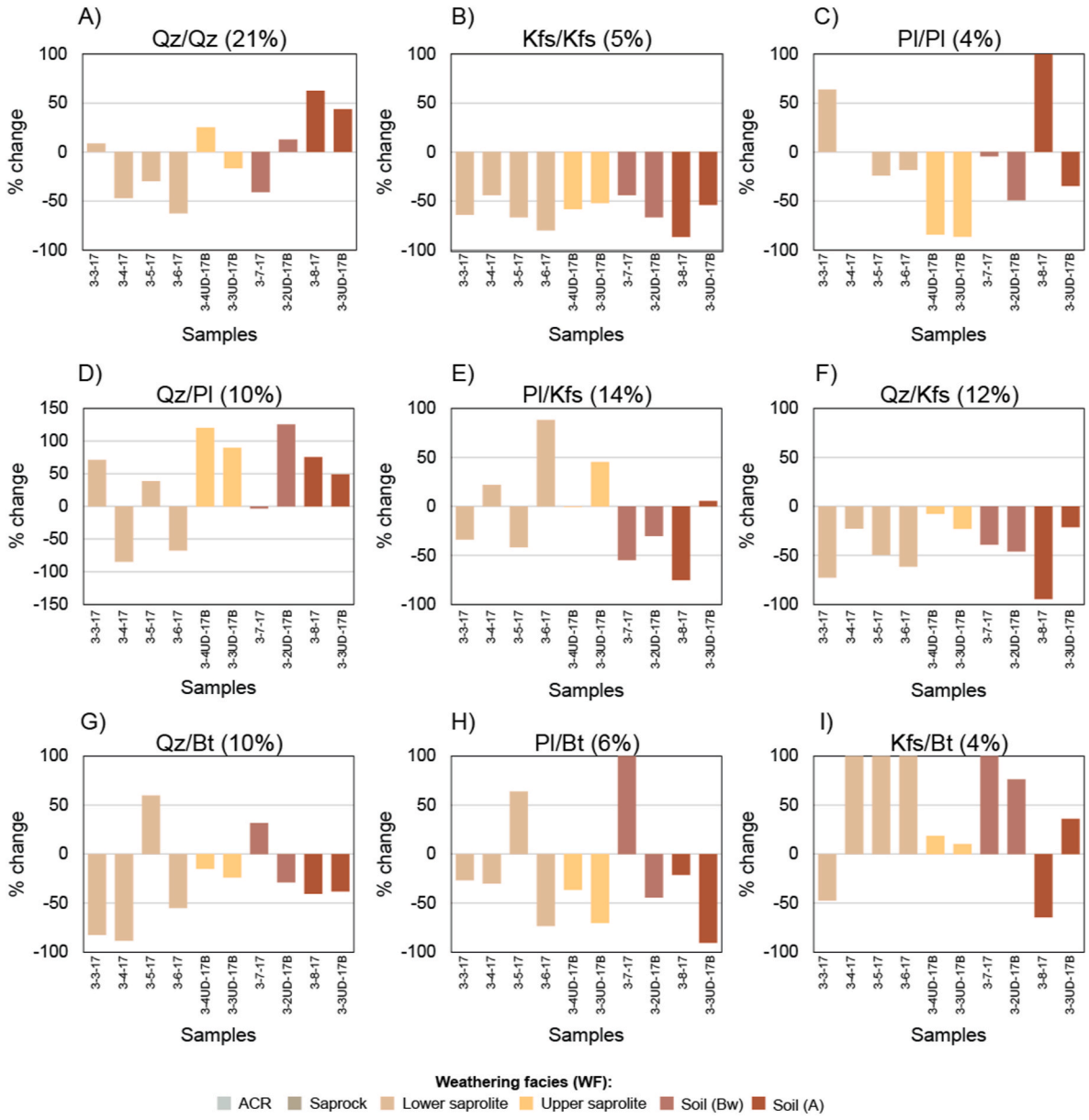

Fig. 10. Percentage changes in major interfaces in relation to the parent material (sample 3-2-17) (See Tables 3 and 4).
A–C: isomineralic interfaces, D–F: anisomineralic and isostructural interfaces, G–I: anisomineralic interfaces involving phyllosilicates. Labels on panel indicate the total fraction of each interface in the assumed protolith sample.

(Fig. 12C). In the five samples from the A horizon, however, both I + M (20–30%) and vermiculite (10–20%) display a trend of increasing amounts upwards at the expense of kaolinite (70–55%) (Tables 6 and 1E, Fig. 12C). In addition, in the A horizon kaolinite is only represented by the ordered polytype, displaying peaks close to 7.15 Å.

4.4. Mass-balance relationships and volumetric changes

4.4.1. Mass-transfer reconstruction for individual elements

Translocation of elements relative to the composition of the parent material (sample 3-20-17B), assuming immobile Al, reveals various trends of losses and gains in the regolith profile (Table 7, Fig. 13).

The concentration of the most abundant element, Si, displays relatively small variations throughout the regolith profile, implying only minimal loss and gains (Fig. 13A).

From the protolith sample (3-20-17B) and up to the sample from the lower saprolite facies (3-15-17B), the Ca concentration experiences a reduction of >50% (Fig. 13E). At the onset of the upper saprolite facies, >80% of the initial Ca has been leached, and the concentration remains stable throughout the saprolite facies and soil B horizon. In the A horizon, a slight increase was observed compared to the underlying B horizon (Fig. 13).

Relative variations of Na, compared to the composition of the protolith displays a comparable but less pronounced trend than the Ca variations (Fig. 13F). Na concentration is reduced by approximately 50% from the ACR to the saprolite facies, but with a slight increase in the soil horizons.

Relative to the composition of the protolith, Mg concentrations experience a drop of about 50% in the saprock facies and are then relatively stable until a slight increase was observed in the soil horizons (Fig. 13D). The trend in Mg concentrations is almost mirrored by the upwards variations in Fe and P (Fig. 13B, H), with a net leaching in the weathered rock and soil Bw horizon, followed by an increase in the soil A horizon. K experiences a large relative gain from the ACR to the

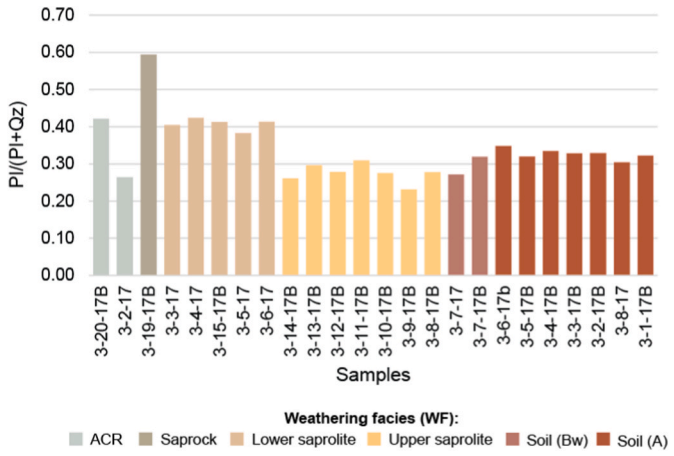

Fig. 11. Pl/(Pl + Qz) ratio from XRD whole rock mineralogy used as mineralogical weathering index (see Table 5).

saprock facies (Fig. 13G). A progressive decrease in K was observed through the lower and upper saprolites and Bw horizon, until stabilising in the A horizon (Fig. 13). Mn experiences a reduction of about 50% in concentration in sample from saprock facies relative to the composition of the assumed protolith. The Mn concentrations remain stable through the saprolite and soil B horizon, but in the soil A horizon, a net gain of >30% is evident (Fig. 13C).

4.4.2. Chemical index of alteration (CIA) and loss on ignition (LOI)

CIA and LOI values both increase progressively upwards through the profile (Table 7, Fig. 14B and C). Possibly due to variations in the original composition, the saprock sample displays a lower CIA value (CIA = 54) than the sample from the ACR facies (CIA = 56). However, the LOI also displays a slight decrease in the saprock facies (Fig. 14C). A small increase in chemical alteration and LOI was observed in the lower saprolite facies compared to the saprock facies. In the upper saprolite facies the CIA and LOI possibly reflect two subsequent units of upwards increasing chemical weathering, almost attaining intermediate degrees of alteration. Intermediate degrees of chemical alteration (CIA>65) are reached in the soil horizons, with the highest recorded CIA being 65.5 (Fig. 14B). The LOI displays a greater relative increase than CIA in the

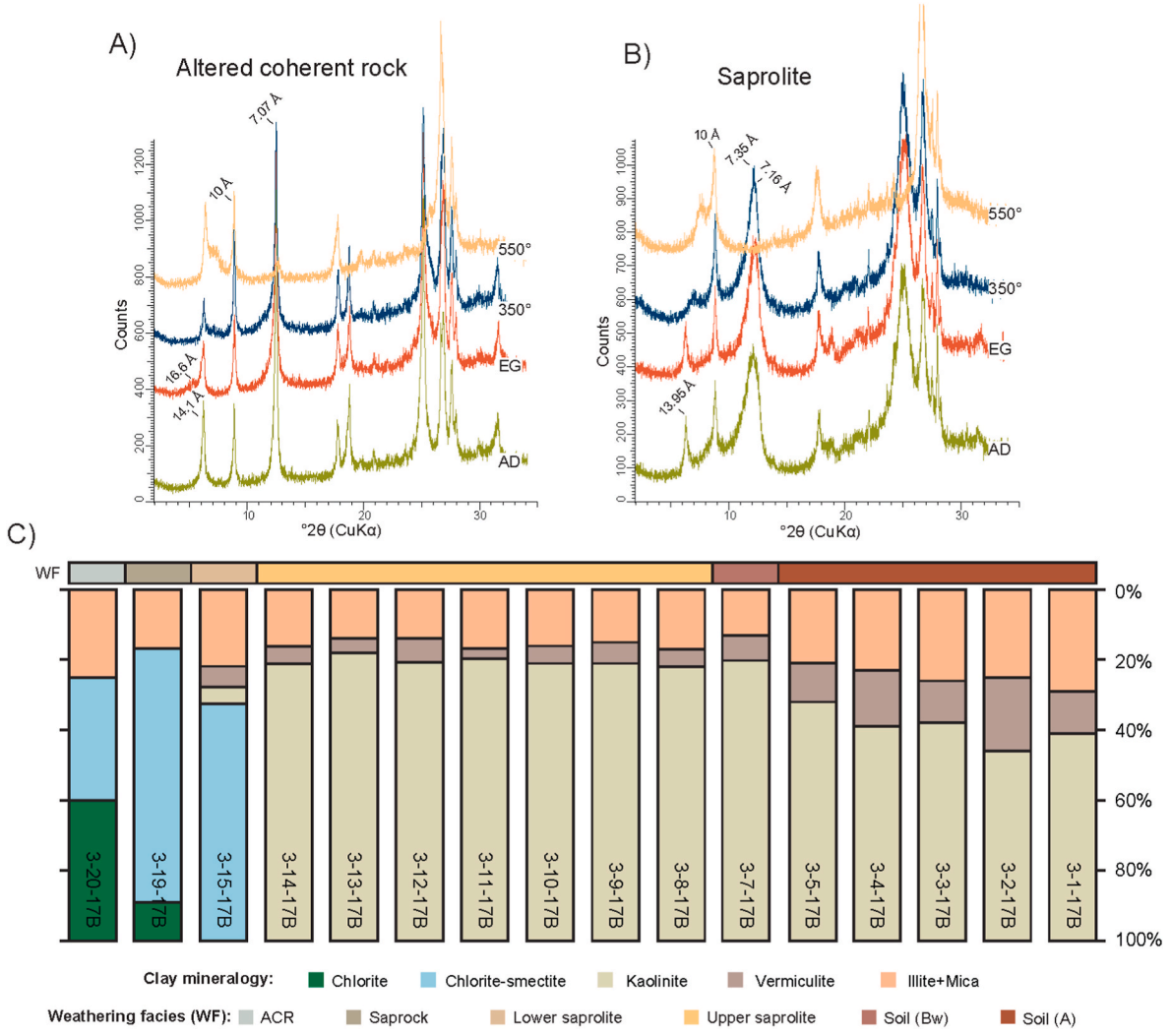

Fig. 12. XRD Clay fraction (see Table 6). A) Clay fraction example from the altered coherent rock facies (ACR), showing diffractograms from air dried (AD), ethylene glycolated (EG), heated at 350° for 1 h and heated at 550° for 1 h.
B) Clay fraction example from the saprolite facies, showing diffractograms from air dried (AD), ethylene glycolated (EG), heated at 350° for 1 h and heated at 550° for 1 h.
C) Chart showing the clay mineralogical composition throughout the studied profile (see Table 6).

Table 7
Major element chemistry[a] and derived parameters for bulk tau (τ_b)[b], bulk density (ρ_b)[c], chemical index of alteration (CIA*)[d] calculated porosity (φ_{calc})[e] and volumetric strain factor (ε)[f].

Sample	Facies	SiO_2	Al_2O_3	Fe_2O_3	MnO	MgO	CaO	Na_2O	K_2O	P_2O_5	LOI	τ_b	ρ_b	CIA*	φ_{calc}	ε
3-1-17B	Soil (A)	64.44	14.64	3.17	0.06	0.75	0.43	1.80	4.27	0.11	10.6	0.02	1.15	64	57	1.36
3-2-17B	Soil (A)	66.4	15.07	3.37	0.06	0.78	0.40	1.89	4.26	0.09	7.64	−0.01	–	65	–	–
3-3-17B	Soil (A)	68.27	14.38	2.83	0.05	0.69	0.36	2.17	4.08	0.09	6.86	0.04	–	63	–	–
3-4-17B	Soil (A)	62.07	15.18	3.59	0.07	0.82	0.47	1.77	3.90	0.13	12.29	−0.02	–	66	–	–
3-5-17B	Soil (A)	64.99	14.57	3.17	0.06	0.73	0.42	1.82	4.06	0.11	10.23	0.02	–	65	–	–
3-6-17B	Soil (A)	65.43	14.62	3.07	0.06	0.78	0.43	2.03	3.84	0.11	9.35	0.02	–	65	–	–
3-7-17B	Soil (A)	71.81	14.16	2.19	0.02	0.56	0.24	2.28	4.63	0.06	3.48	0.05	1.61	61	39	0.74
3-8-17B	Soil (Bw)	71.09	14.90	2.41	0.02	0.63	0.25	1.60	5.54	0.07	3.93	0.00	1.88	63	29	0.42
3-9-17B	Saprolite (U)	71.09	14.61	2.39	0.02	0.62	0.25	1.49	5.79	0.06	3.68	0.02	–	62	–	–
3-10-17B	Saprolite (U)	72.62	14.14	2.25	0.02	0.59	0.23	1.73	5.61	0.07	3.12	0.06	–	61	–	–
3-11-17B	Saprolite (U)	71.47	14.12	2.15	0.02	0.56	0.20	2.00	5.90	0.06	2.85	0.06	1.78	59	33	0.58
3-12-17B	Saprolite (U)	68.73	15.57	3.13	0.03	0.83	0.26	1.46	5.93	0.06	4.03	−0.04	–	63	–	–
3-13-17B	Saprolite (U)	72.32	14.52	2.18	0.02	0.58	0.27	1.85	5.46	0.06	3.3	0.03	–	61	–	–
3-14-17B	Saprolite (U)	73.48	13.37	1.97	0.02	0.52	0.19	1.69	5.79	0.05	3.02	0.12	–	59	–	–
3-15-17B	Saprolite (L)	66.43	16.10	3.01	0.03	0.86	0.59	1.99	7.26	0.15	3.04	−0.07	1.66	58	38	0.48
3-19-17B	Saprock	64.21	18.03	2.64	0.03	0.7	1.02	2.42	8.73	0.17	2.08	−0.17	2.47	55	7	−0.11
3-20-17B	ACR	69.33	14.92	3.89	0.05	1.11	1.38	2.86	3.97	0.18	2.27	0.00	2.66	57	0	0.00

[a] Selected elements reported as %. Total iron reported as Fe_2O_3.
[b] Bulk tau (τ_b) derived from Eq. (2).
[c] For samples 3-1-17B, 3-7-17B, 3-8-17B, 3-11-17B, the reported bulk densities (ρ_b) were obtained from the corresponding undisturbed samples reported in Table 1. For samples 3-15-17B, 3-19-17B and 3-20-17B ρ_b were estimated by volume displacement.
[d] Chemical index of alteration (CIA*) were derived from Eq. (3).
[e] Calculated porosities (φ_{calc}) were determined using Eq. (5).
[f] Volumetric strain factors (ε) were derived from Eq. (6).

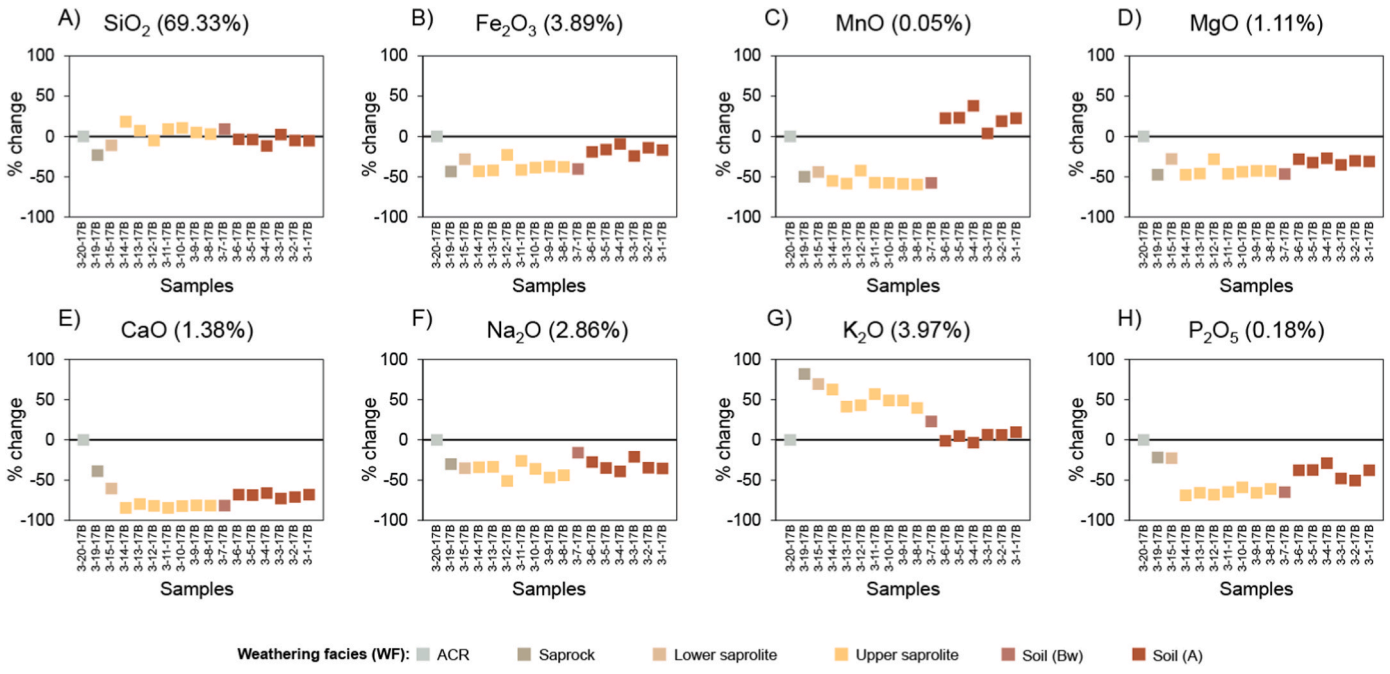

Fig. 13. Changes in individual elements relative to immobile reference element, Al_2O_2. Labels in diagrams indicate weight percentages of elemental oxides in protolith (see Table 7).

organic-rich soils compared to the underlying units (Fig. 14C).

4.4.3. Bulk density (ρ_b), calculated porosity ($\varphi_{c,w}$), bulk mass transfer coefficient (τ_b), and volumetric strain factor (ε)

The measured density (ρ_b) diminishes from 2.66 g/cm^3 in the protolith to 2.47 g/cm^3 in the saprock facies. Furthermore, a gradual density reduction upwards is evident, from 1.66 to 1.88 g/cm^3 in three samples from the saprolite facies, to 1.61 g/cm^3 in the Bw horizon, and 1.15 g/cm^3 in the A-horizon (Fig. 14D).

The corresponding porosities (φ_c) (Eq. (5)) demonstrate values of around 7% in the sample from the saprock facies, increasing to 29–38% in the three samples from the saprolite facies, and to 39% (Bw horizon) and 57% (A-horizon) in the two soil samples (Fig. 14E, Tables 1 and 7).

The upwards tendency in total mass transfer (τ_b) is ambiguous (Table 7, Fig. 14) and indicates that weathering progressed with minimal net gain or loss of mass. The variations in τ_{bulk} mirror the most abundant elemental oxide, SiO_2, and is not reflecting the increasing porosities (Figs. 12 and 13).

The positive and upwards increasing value of the volumetric strain factor (ε) (Fig. 14F) implies that the creation of porosity was primarily the result of enlarged rock volume rather than removal of mass. The volumetric strain factor (ε) indicates an increase in volume of >50% in

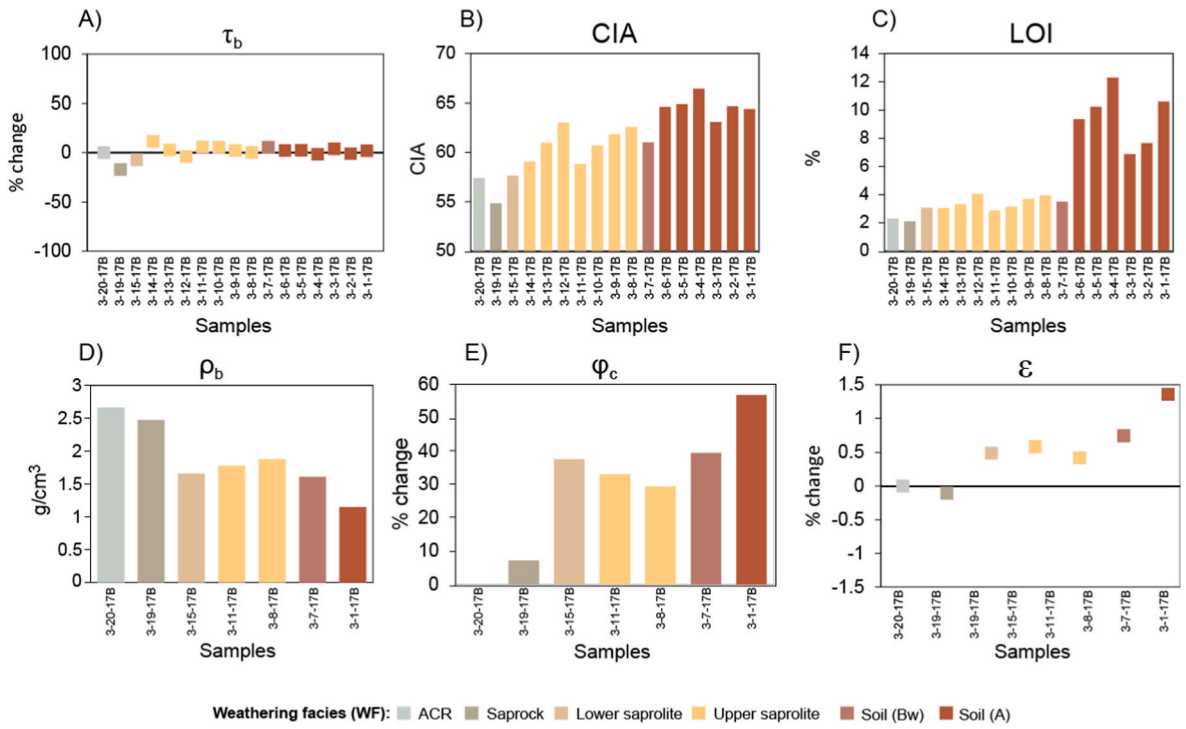

Fig. 14. A) Bulk mass transfer coefficient (τ_{bulk}) indicates very low translocation of mass in the regolith (see Table 7). B) Chemical Index of Alteration (CIA) increases upwards in the regolith, but only reaches intermediate degrees of chemical alteration (CIA = 65, as indicated by dotted line) (see Table 7). C) Loss on Ignition (LOI) suggests an increase in the hydrous phases in the saprolite facies and large amounts of organic matter in the soil horizons (see Table 7). D) Calculated porosity (assuming a grain density of 2.66 and measured p bulk), increases to ~40% in the lower saprolite facies (see Table 7). E) Measured bulk densities (ρ_{bulk}) show a gradual reduction upwards in the regolith (see Table 7). F) Progressive volumetric expansion as indicated by strain factor (ε) (see Table 7).

the saprolite compared to the protolith, while a more than doubling of volume was calculated for the soil sample (Fig. 14F).

5. Discussion

5.1. Hypogene alteration

In fresh – nearly fresh crystalline rocks, alteration advances slowly, with transportation of solutes mainly occurring by diffusion (Bazilevskaya et al., 2015) within thermally or mechanically induced intra- and intermineral micropores (<1% of total rock volume), that were formed by e. g thermal contraction during cooling, by tectonic stresses during stages of deformation, and by stress relaxation during unloading (Kranz, 1983; Schild et al., 2001; Graham et al., 2010). In this study such micropores were observed in the ACR facies. They occur both within quartz crystals and as microfractures following the primary cleavage direction in feldspars. Furthermore, a majority of pre-existing, hypogene microfractures and imperfections were likely healed and sealed by percolating fluids (Schild et al., 2001), but may have been reactivated in the early stages of weathering (Delvigne, 1998). This would have facilitated later infiltration of percolating groundwater (Bergbauer and Martel, 1999; Nelson, 2001; Cuong and Warren, 2009). After reaching the near-surface environment, the fracture tips in the previously formed microfractures may function as reaction sites for fluid/rock interactions in a process of stress corrosion that provokes subcritical fracture propagation (Atkinson and Meredith, 1981; Eppes and Keanini, 2017; Anderson, 2019). Additional hypogene alteration includes the coupled process of replacement of plagioclase with sericite and the chloritisation of biotite, generally attributed to late magmatic metasomatism (Speer, 1984; Eggleton and Banfield, 1985; Que and Allen, 1996).

5.2. Initiation of weathering

Physico-chemical processes are initiated in the Critical Zone (Brantley et al., 2006) when the rock comes into contact with oxygen-rich fluids of meteoric origin (Fletcher et al., 2006), giving rise to:

(1) The transformation and dissolution of primary minerals (Banfield and Eggleton, 1990; Delvigne and Stoops, 1990; White, 1995; White et al., 1998; von Eynatten et al., 2003; Pacheco and Van der Weijden, 2012).
(2) Formation of trans-, intra- and intermineral pores (Bisdom, 1967; Stoops et al., 1979; Vepraskas et al., 1996; Rossi and Graham, 2010; Bazilevskaya et al., 2015; Mazurier et al., 2016; Hayes et al., 2019).
(3) Precipitation of secondary products (Stoops and Delvigne, 1990; Meunier et al., 2007; Bétard et al., 2009).
(4) The removal or addition of elements and material (Brimhall and Dietrich, 1987; Middelburg et al., 1988; Driese et al., 2000; Braun et al., 2009).

In the ACR facies, the CIA value of 56 (Fig. 14) indicates a low degree of chemical alteration (Nesbitt and Young, 1989). Riber et al. (2017) considered the first visible signs of alteration in the ACR facies were the precipitation of ferric oxides along discontinuities, likely sourced from the oxidation of ferrous minerals. Oxidation of Fe (II) and subsequent release as Fe (III) during weathering of biotite has been suggested as an early alteration process in the Critical Zone (Buss et al., 2013; Bazilevskaya et al., 2015). This is the case in the ACR facies in the Sila granodiorites, where >80% of biotite grains are classified as altered, whereas most of the plagioclase (>95%) remain fresh – nearly fresh (Fig. 6). Biotite transformation can progress via intermediate vermiculite, causing expansion in the c-axis direction (Isherwood and Street,

1976; Rebertus et al., 1986; Banfield and Eggleton, 1988; Delvigne and Stoops, 1990; Le Pera and Sorriso-Valvo, 2000; Fletcher et al., 2006; Scarciglia et al., 2007; Bazilevskaya et al., 2013; Parizek and Girty, 2014; Webb and Girty, 2016). In contrast, environments characterised by more aggressive chemical weathering may promote the direct transformation of biotite to kaolinite (Murphy et al., 1998) or even gibbsite (Sequeira Braga and Paquet, 1986). Stress induced by the volumetric increase of biotite crystals may create new sets of micro-fractures that possibly follow cleavage planes of surrounding grains or previously formed zones of weakness (Graham et al., 2010).

During weathering of the Sila granodiorite the first authigenic clay mineral to form was probably the mixed-layered expanding phase (chlorite-smectite) (Fig. 12), which is in accordance with the reaction path model from the same profile (Perri et al., 2015) that predicted smectite (saponite) to be the first mineral to precipitate. The chlorite-smectite mineral is likely the result of incipient transformation of chloritised biotite (Senkayi et al., 1981) and/or neoformed after the alteration of sericitised plagioclase (Taboada and Garcia, 1999) (Fig. 12). The pure chlorite and I + M, identified in the ACR samples, are believed to be inherited from the protoliths (Fig. 12).

From a reservoir perspective, the rock matrix in the ACR facies is a material with poor hydraulic conductivity; the measured density of 2.66 g/cm^3 (Fig. 14) is typical of granitoids with little to no formation of voids (Buss et al., 2008; Hayes et al., 2019), and with the total open pores observed to be less than 2% of the rock volume (Fig. 7). However, macrofractures that are larger than the scale of hand specimens (Fig. 2B) may have been sufficient for transportation and storage of fluids, as is the case in many basement-rock hydrocarbon reservoirs (Cuong and Warren, 2009; Legrand et al., 2011).

5.3. Intermediate stages of weathering

The most eye-catching feature of the saprock facies is the widespread iron oxide staining, while the rock retains its coherence (Fig. 3B). The measured density of 2.47 g/cm^3 is likely related to the increase in observable open pores to about 5% (Figs. 6 and 13). The low degree of chemical alteration is suggested by the CIA of 56 (Fig. 13), however, incipient alteration of plagioclase is suggested by the release of Ca and Na (Fig. 14). In addition, both Fe and Mg were leached due to biotite alteration. Most of the chloritised biotites are pseudomorphically transformed, most likely corresponding to the increase of chlorite-smectite at the expense of chlorite (Fig. 12). The observed opening and interconnection of transecting pores presumptively allowed for increased rates of fluid transportation by advection (Bazilevskaya et al., 2013), and likely accelerated biotite alteration that again promoted reaction-induced fracturing in a self-reinforcing process (Røyne et al., 2008).

5.4. Advanced stages of weathering

The onset of the lower saprolite facies corresponds with a drop in the Pl/(Pl + Qz) ratio (Fig, 11), and the micromorphological observation of altered individual plagioclase crystals (Fig. 6) reflecting the plagioclase reaction front (Bazilevskaya et al., 2015). XRD analysis suggests that the absolute dissolution of plagioclase is minor, and that formation of kaolinite at the expense of plagioclase only results in a clay volume of only about 3% of the total rock (Table 5). CIA track the chemical weathering of feldspars, and the values in the advanced stages of weathering (Fig. 14) suggest incipient – intermediate degrees of chemical alteration (Fedo et al., 1995). The low CIA values are in accordance with the observed conservation of K-feldspar, and the partial preservation of biotite and plagioclase through the advanced stages of weathering (Fig. 6). However, chemical alteration of plagioclase and biotite in the saprolite facies is reflected in the mass balance analysis, showing depletion of Ca, Na, P, Mn, Mg and Fe (Fig. 13). Notwithstanding, these labile elements make up <10% of the parent material (Table 7), and thus their contribution to the overall mass flux are minor, as demonstrated by the small variations in τ_b (Fig. 14). The most abundant element in the parent material, Si (69.33%) (Table 7), is largely immobile through the regolith profile (Fig. 13), and is retained within the primary silicates and secondary clays. These results are in accordance with thermodynamic models by Perri el al. (2015) suggesting close to isochemical weathering processes of the Sila granodiorite at this location. In contrast, in a study of argillaceous weathering under tropical climate in Rio Icacos, Puerto Rico, reported the removal of almost half of the original mass (White et al., 1998; Riebe et al., 2003, 2021). Under such conditions, the high degree of mass removal was likely related to the mobility of Si, in the advanced stages of weathering (Riebe et al., 2003).

The drop in measured density to 1.66 g/cm^3 (Fig. 14D, Table 7) indicates formation of pore space (φ_c = 38%) (Fig. 14E) that, in the absence of major loss of mass, likely involved an increase in rock volume. Total pores observed (φ_{obs}) under the microscope was about 9% and are dominated by transmineral fractures (Figs. 6 and 7). Moderate – strong chemical alteration of individual plagioclase grains presumptively contributed to the opening of grain contacts, as the neoformed material is not occupying the full available volume after the parent mineral (Delvigne, 1998). The well-connected transmineral micro-fractures are for the most part open (Figs. 7 and 9G), except for some infilling of FeOx and neoformed clay films, suggesting the existence of an open pore network that allows increased fluid infiltration. The observed clay coatings may have protected the primary minerals from further chemical weathering (Velde and Meunier, 2008).

The division of the saprolite facies into a lower and upper saprolite was mainly based on the mechanical properties of the rock observed during sampling, but was also reflected in the reduction of Pl/(Pl + Qz) (Fig. 11) and an upwards increase in open pores (Fig. 7). Upwards increase in mineral alteration is evident for both biotite and plagioclase and coincides with the growth of pores (Figs. 5–7). The cracking of individual grains resulted in fragmentation of the primary minerals, thus reducing the overall grain size and increasing the surface area available for chemical reactions (Meunier, 2005). The relative durability of isomineralic interfaces is summarised as Qz/Qz ≫ Kfs/Kfs ≫ Pl/Pl (Fig. 10). Plagioclase is more vulnerable to disintegration because of planes of weakness such as twinning and zoning (e.g., Heins, 1995), indicating a pattern in agreement with that found within the plutoniclastic sand-sized detritus studied by Heins (1995), Caracciolo et al. (2012) and Weltje et al. (2018). Both Bt/Bt and Ms/Ms interfaces appear very sporadic, or are lacking in the upper saprolite samples, indicating comminution towards silt- or clay-size mode (e.g., Slatt and Eyles, 1981; Le Pera and Sorriso-Valvo, 2000; Caracciolo et al., 2012; Weltje et al., 2018).

Furthermore, the open microfracture growth in saprolite with respect to the less weathered rocks, also produces a significant reduction in the effective shear strength and stiffness (Perri et al., 2016). This process, coupled with an increase of hydraulic conductivity, plays an important role in the development of different types of slope instability in the Sila massif and in similar geological settings (Perri et al., 2016).

5.5. Mixture of reworked rock fragments and organic-rich soil

The soil horizons were distinguished by the absence of the original rock texture and high content of organic material. In thin sections, the colluvial material was identified as subrounded rock fragments, implying some transport. The mixture of moderately weathered rock fragments of colluvial origin and clay-rich soil can explain the enhanced Pl/(Pl + Qz) ratios (Fig. 11), and the apparent increase in certain isomineralic and anisomineralic interfaces (Fig. 10), whereas the weathering indices, CIA and LOI, pointed towards more advanced degrees of chemical alteration (Fig. 14), due to the increase in clay content. The drop in K in the soil horizons (Fig. 13) may be related to the uptake of potassium by land plants, rendering K-feldspars unstable and promoting chemical weathering of mineral phases containing such elements in

present-day Sila saprolite particles (Basu, 1981). The partly colluvial soil horizons are dominated by intermineral pores, and the rock fragments display less fracturing than the underlying saprolite (Fig. 8).

5.6. Volumetric strain-inducing processes

Calculated and observed porosities increase as a function of closeness to the surface (Tables 2 and 7, Fig. 14E). The progression in porosities closely follow the calculated growth in volumetric strain (Fig. 14E and F), but appeared less related to the ambiguous τ_{bulk} trend (Fig. 14A). Therefore, the largest fraction of porosity formation is likely a result of volumetric strain inducing processes, with mass loss being subordinate.

Several processes may contribute to the generation of volumetric strain (Parizek and Girty, 2014; Anderson, 2019; Hayes et al., 2019; Riebe et al., 2021):

(1) The study area is located at an elevation of c. 1160 m asl and experiences heavy rainfall and occasional temperatures below freezing during the winter season (Le Pera and Sorriso-Valvo, 2000). Freeze-thaw cycles are a well-known cause of physical weathering, but the phenomenon is not a prerequisite for arenaceous weathering (Sequeira-Braga et al., 1990; Anderson, 2019).
(2) The Calabria region is situated in a complex tectonic area and the Sila Massif has experienced rapid uplift of 0.8–1.1 mm/yr and removal of overburden since the Quaternary (Westaway, 1993), promoting the formation of large-scale fractures that will increase the hydraulic conductivity and hence weathering of the rock (Guzzetta, 1974; Molnar et al., 2007; Navarre-Sitchler et al., 2015; Clair et al., 2015; Novitsky et al., 2018).
(3) Volumetric expansion of Fe-bearing minerals, such as biotite, interacting with oxygenated meteoric waters has been shown both experimentally and as a naturally occurring process (Røyne et al., 2008; Navarre-Sitchler et al., 2015; Røyne and Jamtveit, 2015). Volume change of $\ll$1% can generate stresses high enough to cause cracking of the rock (Røyne and Jamtveit, 2015), and thus mineral expansion as a result of oxidation and subsequent vermiculation of iron rich biotite grains is regarded an important process in arenaceous weathering (Isherwood and Street, 1976; Le Pera and Sorriso-Valvo, 2000; Fletcher et al., 2006; Scarciglia et al., 2007; Buss et al., 2008; Parizek and Girty, 2014; Webb and Girty, 2016; Goodfellow et al., 2016; Kajdas et al., 2017).
(4) It was also likely that the weathering of individual grains, particularly plagioclase, facilitated the progressive opening of fractures in the rock e.g. by weakening Pl/Pl contacts (Fig. 10C), making the two processes mutually dependent, even though one of them may dominate the other under certain conditions.

5.7. Implications for hydrocarbon exploration

In argillaceous regoliths, porosity generally increases upwards, but there is typically a concomitant decrease in permeability due to collapse of the rock structure under its own weight and compaction (Dewandel et al., 2006; Meunier et al., 2007; Velde and Meunier, 2008; Pacheco and Van der Weijden, 2012). Furthermore, the upwards increase in clay content in argillaceous regoliths may occlude permeability by plugging pores and microfractures, or by increasing the length and tortuosity of fluid pathways (Acworth, 1987; Vepraskas et al., 1991, 1996; Wright, 1992; Riber et al., 2017).

Although less studied, the upwards development in permeability in arenaceous regoliths may follow the increasing porosity, as the scarcity of clays allow fluid pathways to remain open even in the advanced stages of weathering (Graham et al., 1997). In a study from the Serre Massif (Calabria, southern Italy) (Fig. 1A), Ietto et al. (2016) analysed fifteen boreholes that penetrated highly weathered arenaceous regoliths and reported an increase in weathering, porosity and permeability with closeness to the surface. These results are in accordance with a study on granitic regoliths from Scandinavia, reporting a positive relationship between permeability and the number of microfractures (Lothe et al., 2018).

Paleo-highs that were subaerially exposed for long times, likely experienced multiple and partly overlapping weathering episodes before burial (Molina et al., 1991; Rosenau et al., 2013). The polygenetic nature of some paleoregoliths may explain why some workers have reported regolith profiles comprising a layer of arenacous saprolites below an argillaceous interval (Jones, 1985; Acworth, 1987; Lachassagne et al., 2011). Therefore, two pore systems with contrasting flow properties may be present in the same vertical regolith profile, and this should be considered when evaluating the reservoir potential for petroleum, groundwater or geothermal fluids in such rocks.

During burial, modification of reservoir properties occur when the confining pressure increases (e.g. Bjørlykke and Høeg, 1997). Experiments on clay rich aggregates have shown that differences in amount and type of clays will influence how porosity and permeability are modified with depth (Mondol et al., 2007), and these relationships may be valid also for buried regoliths (Lothe et al., 2018). When the confining pressure increases, argillaceous regoliths experience greater reduction of porosity and permeability than arenaceous regoliths (Lothe et al., 2018). Furthermore, the larger grain size of kaolinite compared to smectite, suggests that kaolinite rich regoliths are more compressible than regoliths dominated by smectite (Mondol et al., 2007; Lothe et al., 2018). At low confining pressures, the permeability reduction of naturally fractured rocks are dominated by closure of macrofractures, whereas permeability within microfracture networks can be maintained at typical reservoir depths (~2 km burial) (Nara et al., 2011). Thus, it is important to know the type of pore system when predicting evolution of flow properties during burial of regoliths and other fractured reservoir rocks.

6. Conclusions

Two main weathering processes are responsible for the creation of pores in saprolites. In arenaceous saprolites, dilation increases the rock volume whereas in argillaceous saprolites pore creation is dominated by dissolution and removal of material. Arenaceous weathering of the Sila Massif granodiorite, with its closely interlocking crystals, transformed it into altered and disaggregated saprolite and soil. This is an example of how physico-chemical processes interact in certain environments to modify the physical and textural rock properties, producing low to moderate compositional adjustments. Saprolites dominated by arenaceous weathering, as observed in Calabria, can be identified by their mineralogical, geochemical and physical properties. In arenaceous saprolites, weathering progresses by the growth of microfractures and breakage of crystal interfaces, whereas the primary minerals are partially preserved.

Increasing volumetric strain, as expressed by an increase in fracture frequency and aperture, are considered the main cause of pore formation; it was concluded that mass removal is a subordinate process in pore formation in arenaceous saprolites. The well-connected and open microfractures that characterise the pore network in arenaceous saprolites likely improve the hydraulic conductivity of the rock, and permeability may be retained within such microfracture networks at reservoir depths. When evaluating storage capacity and fluid flow in weathered and fractured crystalline rocks, a deep understanding of the alteration history and pore development is vital.

Credit author statement

Lars Riber: Conceptualization, Methodology, Formal analysis, Writing – Original Draft, Writing- Review and Editing, Funding acquisition, Visualization, Investigation.

Emilia Le Pera: Supervision, Project Administration,

Conceptualization, Methodology, Writing – Original Draft, Writing- Review and Editing, Formal analysis, Validation, Resources, Investigation.

Consuele Morrone: Formal analysis, Writing- Review and Editing, Investigation, Validation.

Fabio Ietto: Writing- Review and Editing, Resources, Investigation.

Massimo Conforti: Formal analysis, Validation, Writing- Review and Editing, Resources, Investigation.

Henning Dypvik: Supervision, Project Administration, Methodology, Writing- Review and Editing, Investigation.

Declaration of competing interest

The authors declare that they have no known competing financial interests or personal relationships that could have appeared to influence the work reported in this paper.

Acknowledgements

Funding for LR was made available by Lundin Energy (Norway), and by the Suprabasins project (RCN# 295208) supported by the Norwegian Research Council and industry partners Aker BP, Spirit Energy, Equinor and Lundin Energy. LR thanks S. Munch, D.M. Nordhagen and L. Lundh for the discussions and inputs when writing this manuscript. We thank Siri Simonsen and Salahalldin Akhavan at the Department of Geosciences, University of Oslo for assistance during SEM analysis and thin section preparations. Thanks to Adrian J. Read for proofreading the manuscript. Lastly, the authors acknowledge the very constructive reviews by José Arribas, Luca Barale and one anonymous reviewer, which improved the manuscript greatly.

References

Abdelazim, R., Rahman, S.S., 2016. Estimation of permeability of naturally fractured reservoirs by pressure transient analysis: an innovative reservoir characterization and flow simulation. J. Petrol. Sci. Eng. 145, 404–422.
Acworth, R., 1987. The development of crystalline basement aquifers in a tropical environment. Q. J. Eng. Geol. Hydrogeol. 20, 265–272.
Amodio-Morelli, L., Bonardi, G., Colonna, V., Dietrich, D., Giunta, G., Ippolito, F., Liguori, V., Lorenzoni, S., Paglionico, A., Perrone, V., PIccarreta, G., Russo, M., Scandone, P., Zanettin Lorenzoni, E., Zuppetta, A., 1976. L'arco Calabro-Peloritano nell'orogene appenninico-maghrebide. Memoirs della Società geologica italiana 17, 1–60.
Anderson, S.P., 2019. Breaking it down: mechanical processes in the weathering engine. Elements 15, 247–252.
Areshev, E., Dong, T.L., San, N.T., Shnip, O., 1992. Reservoirs in fractured basement on the continental shelf of southern Vietnam. J. Petrol. Geol. 15, 451–464.
Atkinson, B.K., Meredith, P.G., 1981. Stress corrosion cracking of quartz: a note on the influence of chemical environment. Tectonophysics 77, T1–T11.
Bailey, E.H., Stevens, R.E., 1960. Selective staining of K-feldspar and plagioclase on rock slabs and thin sections. Am. Mineral.: J. Earth Planet. Mater. 45, 1020–1025.
Banfield, J.F., Eggleton, R.A., 1988. Transmission electron microscope study of biotite weathering. Clay Clay Miner. 36, 47–60.
Banfield, J.F., Eggleton, R.A., 1990. Analytical transmission electron microscope studies of plagioclase, muscovite, and K-feldspar weathering. Clay Clay Miner. 38, 77–89.
Basu, A., 1981. Weathering before the advent of land plants: evidence from unaltered detrital K-feldspars in Cambrian-Ordovician arenites. Geology 9, 132–133.
Bazilevskaya, E., Lebedeva, M., Pavich, M., Rother, G., Parkinson, D.Y., Cole, D., Brantley, S.L., 2013. Where fast weathering creates thin regolith and slow weathering creates thick regolith. Earth Surf. Process. Landforms 38, 847–858.
Bazilevskaya, E., Rother, G., Mildner, D.F., Pavich, M., Cole, D., Bhatt, M.P., Jin, L., Steefel, C.I., Brantley, S.L., 2015. How oxidation and dissolution in diabase and granite control porosity during weathering. Soil Sci. Soc. Am. J. 79, 55–73.
Begonha, A., Sequeira Braga, M.A., 2002. Weathering of the Oporto granite: geotechnical and physical properties. Catena 49, 57–76.
Bergbauer, S., Martel, S.J., 1999. Formation of joints in cooling plutons. J. Struct. Geol. 21, 821–835.
Bétard, F., Caner, L., Gunnell, Y., Bourgeon, G., 2009. Illite neoformation in plagioclase during weathering: evidence from semi-arid Northeast Brazil. Geoderma 152, 53–62.
Biondino, D., Borrelli, L., Critelli, S., Muto, F., Apollaro, C., Coniglio, S., Tripodi, V., Perri, F., 2020. A multidisciplinary approach to investigate weathering processes affecting gneissic rocks (Calabria, southern Italy). Catena 187, 104372.
Bisdom, E., 1967. The role of micro-crack systems in the spheroidal weathering of an intrusive granite in Galicia (NW Spain). Geol. Mijnbouw 46, 333–340.
Bjørlykke, K., Høeg, K., 1997. Effects of burial diagenesis on stresses, compaction and fluid flow in sedimentary basins. Mar. Petrol. Geol. 14, 267–276.
Borrelli, L., Perri, F., Critelli, S., Gullà, G., 2012. Minero-petrographical features of weathering profiles in Calabria, southern Italy. Catena 92, 196–207.
Borrelli, L., Perri, F., Critelli, S., Gullà, G., 2014. Characterization of granitoid and gneissic weathering profiles of the Mucone River basin (Calabria, southern Italy). Catena 113, 325–340.
Boutt, D.F., Diggins, P., Mabee, S., 2010. A field study (Massachusetts, USA) of the factors controlling the depth of groundwater flow systems in crystalline fractured-rock terrain. Hydrogeol. J. 18, 1839–1854.
Braathen, A., Abdel Fattah, M.M., Olaussen, S., Abdel-Gawad, G., Ogata, K., 2018. Basement–cover reservoir analogue in rift-margin fault blocks; Gulf of Suez Rift, Sinai, Egypt. Petrol. Geosci. 24, 449–468.
Brantley, S., White, T., White, A., Sparks, D., Richter, D., Pregitzer, K., Derry, L., Chorover, J., Chadwick, O., April, R., 2006. Frontiers in Exploration of the Critical Zone: Report of a Workshop Sponsored by the National Science Foundation (NSF). October 24–26, 2005. Newark, DE 30.
Braun, J.-J., Descloitres, M., Riotte, J., Fleury, S., Barbiéro, L., Boeglin, J.-L., Violette, A., Lacarce, E., Ruiz, L., Sekhar, M., 2009. Regolith mass balance inferred from combined mineralogical, geochemical and geophysical studies: mule Hole gneissic watershed, South India. Geochem. Cosmochim. Acta 73, 935–961.
Brimhall, G.H., Dietrich, W.E., 1987. Constitutive mass balance relations between chemical composition, volume, density, porosity, and strain in metasomatic hydrochemical systems: results on weathering and pedogenesis. Geochem. Cosmochim. Acta 51, 567–587.
Buss, H.L., Sak, P.B., Webb, S.M., Brantley, S.L., 2008. Weathering of the Rio Blanco quartz diorite, luquillo Mountains, Puerto Rico: coupling oxidation, dissolution, and fracturing. Geochem. Cosmochim. Acta 72, 4488–4507.
Buss, H.L., Brantley, S.L., Scatena, F., Bazilievskaya, E., Blum, A., Schulz, M., Jiménez, R., White, A.F., Rother, G., Cole, D., 2013. Probing the deep critical zone beneath the luquillo experimental forest, Puerto Rico. Earth Surf. Process. Landforms 38, 1170–1186.
Buss, H.L., Lara, M.C., Moore, O.W., Kurtz, A.C., Schulz, M.S., White, A.F., 2017. Lithological influences on contemporary and long-term regolith weathering at the Luquillo Critical Zone Observatory. Geochem. Cosmochim. Acta 196, 224–251.
Caracciolo, L., Tolosana-Delgado, R., Le Pera, E., Von Eynatten, H., Arribas, J., Tarquini, S., 2012. Influence of granitoid textural parameters on sediment composition: implications for sediment generation. Sediment. Geol. 280, 93–107.
Cather, S.M., Folk, R.L., 1991. Pre-diagenetic sedimentary fractionation of andesitic detritus in a semi-arid climate: an example from the eocene datil group, New Mexico. In: Fisher, R.V., Smith, G.A. (Eds.), Sedimentation in Volcanic Settings. SEPM Society for Sediment. Geol., pp. 211–226
Chilton, P.J., Foster, S.S.D., 1995. Hydrogeological characterisation and water-supply potential of basement aquifers in tropical Africa. Hydrogeol. J. 3, 36–49.
Clair, J.S., Moon, S., Holbrook, W.S., Perron, J.T., Riebe, C.S., Martel, S.J., Carr, B., Harman, C., Singha, K., Richter, D.deB., 2015. Geophysical imaging reveals topographic stress control of bedrock weathering. Science 350, 534–538.
Critelli, S., Le Pera, E., 1998. Post-Oligocene sediment-dispersal systems and unroofing history of the Calabrian microplate. Italy. Int. Geol. Rev. 40, 609–637.
Cuong, T.X., Warren, J., 2009. Bach ho field, a fractured granitic basement reservoir, Cuu Long Basin, offshore SE Vietnam: a "buried-hill" play. J. Petrol. Geol. 32, 129–156.
Delvigne, J.E., 1998. Atlas of Micromorphology of Mineral Alteration and Weathering. Mineralogical Association of Canada, Ottawa, Ontario, Canada, p. 494.
Delvigne, J., Stoops, G., 1990. Morphology of Mineral Weathering and Neoformation. I. Weathering of Most Common Silicates. Dev. Soil Sci. Elsevier, pp. 471–481.
Dewandel, B., Lachassagne, P., Wyns, R., Maréchal, J.C., Krishnamurthy, N.S., 2006. A generalized 3-D geological and hydrogeological conceptual model of granite aquifers controlled by single or multiphase weathering. J. Hydrol 330 (1–2), 260–284.
Doebelin, N., Kleeberg, R., 2015. Profex: a graphical user interface for the Rietveld refinement program BGMN. J. Appl. Crystallogr. 48, 1573–1580.
Driese, S.G., Mora, C.I., Stiles, C.A., Joeckel, R., Nordt, L.C., 2000. Mass-balance reconstruction of a modern Vertisol: implications for interpreting the geochemistry and burial alteration of paleo-Vertisols. Geoderma 95, 179–204.
Ebigbo, A., Niederau, J., Marquart, G., Dini, I., Thorwart, M., Rabbel, W., Clauser, C., 2016. Influence of depth, temperature, and structure of a crustal heat source on the geothermal reservoirs of Tuscany: numerical modelling and sensitivity study. Geoth. Energy 4, 1–29.
Eggleton, R.A., Banfield, J.F., 1985. The alteration of granitic biotite to chlorite. Am. Mineral. 70, 902–910.
Eppes, M.C., Keanini, R., 2017. Mechanical weathering and rock erosion by climate-dependent subcritical cracking. Rev. Geophys. 55, 470–508.
Faccenna, C., Becker, T.W., Lucente, F.P., Jolivet, L., Rossetti, F., 2001. History of subduction and back arc extension in the Central Mediterranean. Geophys. J. Int. 145, 809–820.
Farquharson, J.I., Kushnir, A.R., Wild, B., Baud, P., 2020. Physical property evolution of granite during experimental chemical stimulation. Geoth. Energy 8, 1–24.
Fedo, C.M., Nesbitt, H.W, Young, G.M., 1995. Unraveling the effects of potassium metasomatism in sedimentary rocks and paleosols, with implications for paleoweathering conditions and provenance. Geology 23, 921–924.
Fletcher, R., Buss, H.L., Brantley, S.L., 2006. A spheroidal weathering model coupling porewater chemistry to soil thicknesses during steady-state denudation. Earth Planet Sci. Lett. 244, 444–457.
Foster, S., 2012. Hard-rock aquifers in tropical regions: using science to inform development and management policy. Hydrogeol. J. 20, 659–672.
Fredin, O., Viola, G., Zwingmann, H., Sørlie, R., Brönner, M., Lie, J.-E., Grandal, E.M., Müller, A., Margreth, A., Vogt, C., 2017. The inheritance of a Mesozoic landscape in western Scandinavia. Nat. Commun. 8, 1–11.

George, R.J., 1992. Hydraulic properties of groundwater systems in the saprolite and sediments of the wheatbelt, Western Australia. J. Hydrol. 130, 251–278.
Goodfellow, B.W., Hilley, G.E., Webb, S.M., Sklar, L.S., Moon, S., Olson, C.A., 2016. The chemical, mechanical, and hydrological evolution of weathering granitoid. J. Geophys. Res. Earth 121, 1410–1435.
Graham, R., Anderson, M., Sternberg, P., Tice, K., Schoeneberger, P., 1997. Morphology, porosity, and hydraulic conductivity of weathered granitic bedrock and overlying soils. Soil Sci. Soc. Am. J. 61, 516–522.
Graham, R.C., Rossi, A.M., Hubbert, K.R., 2010. Rock to regolith conversion: producing hospitable substrates for terrestrial ecosystems. GSA Today (Geol. Soc. Am.) 20, 5.
Gutmanis, J.C., 2009. Basement reservoirs - a review of their geological and production characteristics. In: IPTC 2009: International Petroleum Technology Conference. European Association of Geoscientists & Engineers, Doha, Qatar, 7 - 9 Dec 2009.
Guzzetta, G., 1974. Ancient tropical weathering in Calabria. Nature 251, 302–303.
Hayes, J.L., Riebe, C.S., Holbrook, W.S., Flinchum, B.A., Hartsough, P.C., 2019. Porosity production in weathered rock: where volumetric strain dominates over chemical mass loss. Sci. Adv. 5, 1–11.
Heins, W.A., 1993. Source rock texture versus climate and topography as controls on the composition of modern, plutoniclastic sand. In: Johnsson, M.J., Basu, A. (Eds.), Processes Controlling the Composition of Clastic Sediments: Boulder Colorado. Geol. S. Am. S., pp. 135–146
Heins, W.A., 1995. The use of mineral interfaces in sand-sized rock fragments to infer ancient climate. Geol. Soc. Am. Bull. 107, 113–125.
Ietto, F., Perri, F., Cella, F., 2016. Geotechnical and landslide aspects in weathered granitoid rock masses (Serre Massif, southern Calabria, Italy). Catena 145, 301–315.
Isherwood, D., Street, A., 1976. Biotite-induced grussification of the boulder creek granodiorite, boulder county, Colorado. Geol. Soc. Am. Bull. 87, 366–370.
James, W.C., Mack, G.H., Suttner, L.J., 1981. Relative alteration of microcline and sodic plagioclase in semi-arid and humid climates. J. Sediment. Res. 51, 151–164.
Jones, M.J., 1985. The weathered zone aquifers of the basement complex areas of Africa. Q. J. Eng. Geol. 18, 35–46.
Kajdas, B., Michalik, M.J., Migoń, P., 2017. Mechanisms of granite alteration into grus, Karkonosze granite, SW Poland. Catena 150, 230–245.
Klee, J., Potel, S., Ledésert, B.A., Hébert, R.L., Chabani, A., Barrier, P., Trullenque, G., 2021. Fluid-rock interactions in a paleo-geothermal reservoir (noble hills granite, California, USA). Part 1: granite pervasive alteration processes away from fracture zones. Geosci. 11, 325.
Kranz, R.L., 1983. Microcracks in rocks: a review. Tectonophysics 100, 449–480.
Lachassagne, P., Wyns, R., Dewandel, B., 2011. The fracture permeability of hard rock aquifers is due neither to tectonics, nor to unloading, but to weathering processes. Terra. Nova 23, 145–161.
Lachassagne, P., Dewandel, B., Wyns, R., 2021. Hydrogeology of weathered crystalline/hard-rock aquifers—guidelines for the operational survey and management of their groundwater resources. Hydrogeol. J. 29, 2561–2594.
Le Pera, E., Sorriso-Valvo, M., 2000. Weathering and morphogenesis in a mediterranean climate, Calabria, Italy. Geomorphology 34, 251–270.
Le Pera, E., Critelli, S., Sorriso-Valvo, M., 2001. Weathering of gneiss in Calabria, southern Italy. Catena 42, 1–15.
Le Pera, E., Morrone, C., 2020. The use of mineral interfaces in sand-sized volcanic rock fragments to infer mechanical durability. J. Palaeogeogr. 9, 1–26.
Legrand, N., De Kok, J., Neff, P., Clemens, T., 2011. Recovery mechanisms and oil recovery from a tight, fractured basement reservoir, Yemen. In: Paper Presented at the SPE Annual Technical Conference and Exhibition, Florence, Italy, September 2010. Soc. Petrol. Eng., pp. 493–504
Le Van Hung, L., Farag, S.M., Mas, C., Maizeret, P.-D., Li, B., Dang, T., 2009. Advances in granitic basement reservoir evaluation. In: Paper presented at the Asia Pacific Oil and Gas Conference & Exhibition, Jakarta, Indonesia, August 2009. Soc. Petrol. Eng., pp. 1–15
Lie, J.E., Nilsen, E.H., Grandal, E., Grue, K., Sørlie, R., 2016. A successful geophysical prediction of fractured porous basement reservoir - rolvsnes oil discovery 2015, Utsira high. In: Proceedings of the 78th EAGE Conference and Exhibition. May 2016.
Lothe, A.E., Emmel, B., Bergmo, P., Akervoll, I., Todorovic, J., Bhuiyan, M., Knies, J., 2018. Porosity, permeability and compaction trends for Scandinavian regoliths. Mar. Petrol. Geol. 92, 319–331.
Maesano, F.E., Tiberti, M.M., Basili, R., 2017. The Calabrian Arc: three-dimensional modelling of the subduction interface. Sci. Rep. -UK 7, 1–15.
Mazurier, A., Sardini, P., Rossi, A.M., Graham, R.C., Hellmuth, K.-H., Parneix, J.-C., Siitari-Kauppi, M., Voutilainen, M., Caner, L., 2016. Development of a fracture network in crystalline rocks during weathering: study of Bishop Creek chronosequence using X-ray computed tomography and 14C-PMMA impregnation method. GSA Bull. 128, 1423–1438.
McLennan, S.M., 1993. Weathering and global denudation. J. Geol. 101, 295–303.
Mertens, G., Reynolds III, R.R., Adriaens, R.R., 2016. NEWMOD-2-A Computer Program for Qualitative and Quantitative 1-D X-Ray Diffraction Pattern Modeling, Fifth EAGE Shale Workshop. European Association of Geoscientists & Engineers, pp. 1–3.
Messina, A., Compagnoni, R., De Vivo, B., Perrone, V., Russo, S., 1991. Geological and petrochemical study of the Sila massif plutonic rocks (northern Calabria, Italy). Boll. Soc. Geol. Ital. 110, 165–206.
Meunier, A., Velde, B.D., Dudoignon, P., Beaufort, D., 1983. Identification of weathering and hydrothermal alteration in acidic rocks: petrography and mineralogy of clay minerals. Sciences Géologiques, Bulletins et mémoires 72, 93–99.
Meunier, A., 2005. Clays. Springer Science & Business Media, p. 472.
Meunier, A., Sardini, P., Robinet, J., Prêt, D., 2007. The petrography of weathering processes: facts and outlooks. Clay Miner. 42, 415–435.
Middelburg, J.J., van der Weijden, C.H., Woittiez, J.R., 1988. Chemical processes affecting the mobility of major, minor and trace elements during weathering of granitic rocks. Chem. Geol. 68, 253–273.
Migoń, P., Lidmar-Bergström, K., 2001. Weathering mantles and their significance for geomorphological evolution of central and northern Europe since the Mesozoic. Earth Sci. Rev. 56, 285–324.
Migoń, P., Thomas, M.F., 2002. Grus weathering mantles—problems of interpretation. Catena 49, 5–24.
Molina, E., González, M.G., Espejo, R., 1991. Study of paleoweathering on the Spanish hercynian basement Montes de Toledo (Central Spain). Catena 18, 345–354.
Molnar, P., Anderson, R.S., Anderson, Prestrud, S., 2007. Tectonics, fracturing of rock, and erosion. J. Geophys. Res. Earth 112.
Mondol, N.H., Bjørlykke, K., Jahren, J., Høeg, K., 2007. Experimental mechanical compaction of clay mineral aggregates—changes in physical properties of mudstones during burial. Mar. Petrol. Geol. 24 (5), 289–311.
Mongelli, G., Cullers, R.L., Dinelli, E., Rottura, A., 1998. Elemental Mobility during the Weathering of Exposed Lower Crust: the Kinzigitic Paragneisses from the Serre, Calabria, vol. 10. Southern Italy. Terra Nova, pp. 190–195.
Moore, D.M., Reynolds Jr., R.C., 1997. X-ray Diffraction and the Identification and Analysis of Clay Minerals. Oxford University Press (OUP).
Moresi, M., 1987. L'alterazione dei graniti delle Serre orientali (Calabria). Rendiconti della Soc. Ital. Mineral. Petrol. 42, 237–248.
Murphy, S.F., Brantley, S.L., Blum, A.E., White, A.F., Dong, H., 1998. Chemical weathering in a tropical watershed, Luquillo Mountains, Puerto Rico: II. Rate and mechanism of biotite weathering. Geochem. Cosmochim. Acta 62, 227–243.
Murray, A., Montgomery, D.W., 2014. Characterization of highly fractured basement, Say'un Masila Basin. Yemen. Geol. Soc., London, Spec. Publ. 374, 289–310.
Nara, Y., Meredith, P.G., Yoneda, T., Kaneko, K., 2011. Influence of macro-fractures and micro-fractures on permeability and elastic wave velocities in basalt at elevated pressure. Tectonophysics 503 (1–2), 52–59.
Navarre-Sitchler, A.K., Cole, D.R., Rother, G., Jin, L., Buss, H.L., Brantley, S.L., 2013. Porosity and surface area evolution during weathering of two igneous rocks. Geochem. Cosmochim. Acta 109, 400–413.
Navarre-Sitchler, A., Brantley, S.L., Rother, G., 2015. How porosity increases during incipient weathering of crystalline silicate rocks. Rev. Mineral. Geochem. 80, 331–354.
Nelson, R., Moldovanyi, E., Matcek, C., Azpiritxaga, I., Bueno, E., 2000. Production characteristics of the fractured reservoirs of the La Paz field, Maracaibo Basin, Venezuela. AAPG Bull. 84, 1791–1809.
Nelson, R., 2001. Geologic Analysis of Naturally Fractured Reservoirs. Elsevier, p. 331.
Nesbitt, H., Young, G., 1982. Early Proterozoic climates and plate motions inferred from major element chemistry of lutites. Nature 299, 715–717.
Nesbitt, H., Young, G.M., 1989. Formation and diagenesis of weathering profiles. J. Geol. 97, 129–147.
Njueya, A.K., Kengni, L., Fonteh, M.F., David Nkouathio, G., Mebo, S.M.B., 2022. Characterization of aquifers and hydrogeochemical processes in Ngaoundéré, Adamawa region, Cameroon. Arabian J. Geosci. 15 (11), 1–16.
Novitsky, C.G., Holbrook, W.S., Carr, B.J., Pasquet, S., Okaya, D., Flinchum, B.A., 2018. Mapping inherited fractures in the critical zone using seismic anisotropy from circular surveys. Geophys. Res. Lett. 45, 3126–3135.
Ottesen, S., Selvikvåg, B., Scott, A.S., Meneguolo, R., Cullum, A., Amilibia-Cabeza, A., Vigorito, M., Helsem, A., Martinsen, O.J., 2022. Geology of the Johan Sverdrup field: a giant oil discovery and development project in a mature Norwegian North Sea basin. AAPG Bull. 106, 897–936.
Pacheco, F.A., Alencoão, A.M., 2006. Role of fractures in weathering of solid rocks: narrowing the gap between laboratory and field weathering rates. J. Hydrol. 316, 248–265.
Pacheco, F.A., Van der Weijden, C.H., 2012. Weathering of plagioclase across variable flow and solute transport regimes. J. Hydrol. 420, 46–58.
Palomares, M., Arribas, J., 1993. Modern stream sands from compound crystalline sources: composition and sand generation index. In: Johnsson, M., Basu, A. (Eds.), Processes Controlling the Composition of Clastic Sediments: Boulder, Colorado. Geol. S. Am. S., pp. 313–322
Parizek, J.R., Girty, G.H., 2014. Assessing volumetric strains and mass balance relationships resulting from biotite-controlled weathering: implications for the isovolumetric weathering of the Boulder Creek Granodiorite, Boulder County, Colorado, USA. Catena 120, 29–45.
Parneix, J., Beaufort, D., Dudoignon, P., Meunier, A., 1985. Biotite chloritization process in hydrothermally altered granites. Chem. Geol. 51, 89–101.
Perri, F., Scarciglia, F., Apollaro, C., Marini, L., 2015. Characterization of granitoid profiles in the Sila Massif (Calabria, southern Italy) and reconstruction of weathering processes by mineralogy, chemistry, and reaction path modeling. J. Soils Sediments 15, 1351–1372.
Perri, F., Ietto, F., Le Pera, E., Apollaro, C., 2016. Weathering processes affecting granitoid profiles of Capo Vaticano (Calabria, southern Italy) based on petrographic, mineralogic and reaction path modelling approaches. Geol. J. 51, 368–386.
Que, M., Allen, A.R., 1996. Sericitization of plagioclase in the Rosses granite complex, Co. Donegal, Ireland. Mineral. Mag. 60, 927–936.
Rebertus, R., Weed, S., Buol, S., 1986. Transformations of biotite to kaolinite during saprolite-soil weathering. Soil Sci. Soc. Am. J. 50, 810–819.
Regassa, A., Van Daele, K., De Paepe, P., Dumon, M., Deckers, J., Asrat, A., Van Ranst, E., 2014. Characterizing weathering intensity and trends of geological materials in the Gilgel Gibe catchment, southwestern Ethiopia. J. Afr. Earth Sci. 99, 568–580.
Riber, L., Dypvik, H., Sørlie, R., 2015. Altered basement rocks on the Utsira high and its surroundings, Norwegian North Sea. Nor. J. Geol. 95, 57–89.

Riber, L., Dypvik, H., Sørlie, R., Ferrell Jr., R.E., 2016. Clay minerals in deeply buried paleoregolith profiles, Norwegian North Sea. Clay Clay Miner. 64, 588–607.
Riber, L., Dypvik, H., Sørlie, R., Naqvi, S.A.A.-E.-M., Stangvik, K., Oberhardt, N., Schroeder, P.A., 2017. Comparison of deeply buried paleoregolith profiles, Norwegian North Sea, with outcrops from southern Sweden and Georgia, USA—implications for petroleum exploration. Palaeogeogr. Palaeocl. 471, 82–95.
Riber, L., Driese, S.G., Stinchcomb, G.E., Dypvik, H., Sørlie, R., 2019. Reconstructing a high paleolatitude Mesozoic paleoenvironment from a truncated and deeply buried regolith, Norwegian North Sea. Palaeogeogr. Palaeocl. 528, 60–77.
Riebe, C.S., Kirchner, J.W., Finkel, R.C., 2003. Long-term rates of chemical weathering and physical erosion from cosmogenic nuclides and geochemical mass balance. Geochem. Cosmochim. Acta 67, 4411–4427.
Riebe, C.S., Callahan, R.P., Granke, S.B.-M., Carr, B.J., Hayes, J.L., Schell, M.S., Sklar, L. S., 2021. Anisovolumetric weathering in granitic saprolite controlled by climate and erosion rate. Geology 49, 551–555.
Rietveld, H.M., 1969. A profile refinement method for nuclear and magnetic structures. J. Appl. Crystallogr. 2, 65–71.
Rosenau, N.A., Tabor, N.J., Elrick, S.D., Nelson, W.J., 2013. Polygenetic history of paleosols in middle–upper Pennsylvanian cyclothems of the Illinois basin, USA: Part I. Characterization of paleosol types and interpretation of pedogenic processes. J. Sediment. Res. 83, 606–636.
Rossi, A.M., Graham, R.C., 2010. Weathering and porosity formation in subsoil granitic clasts, Bishop Creek moraines, California. Soil Sci. Soc. Am. J. 74, 172–185.
Rønnevik, H.C., Jørstad, A., Lie, J.E., 2017. The discovery process behind the giant johan sverdrup field. In: Merrill, R.K., Sternbach, C.A. (Eds.), Giant Fields of the Decade 2000-2010. AAPG Memoir, pp. 195–220.
Røyne, A., Jamtveit, B., 2015. Pore-scale controls on reaction-driven fracturing. Rev. Mineral. Geochem. 80, 25–44.
Røyne, A., Jamtveit, B., Mathiesen, J., Malthe-Sørenssen, A., 2008. Controls on rock weathering rates by reaction-induced hierarchical fracturing. Earth Planet Sci. Lett. 275, 364–369.
Salah, M., Alsharhan, A., 1998. The Precambrian basement: a major reservoir in the rifted basin, Gulf of Suez. J. Petrol. Sci. Eng. 19, 201–222.
Santos, J.C.B.D., Le Pera, E., de Souza Júnior, V.S., de Oliveira, C.S., Juilleret, J., Corrêa, M.M., de Azevedo, A.C., 2018. Porosity and genesis of clay in gneiss saprolites: the relevance of saprolithology to whole regolith pedology. Geoderma 319, 1–13.
Sausse, J., Genter, A., 2005. Types of Permeable Fractures in Granite, vol. 240. Geol. Soc., London, S, pp. 1–14.
Scarciglia, F., Le Pera, E., Critelli, S., 2005. Weathering and pedogenesis in the Sila grande massif (Calabria, south Italy): from field scale to micromorphology. Catena 61, 1–29.
Scarciglia, F., Le Pera, E., Critelli, S., 2007. The onset of the sedimentary cycle in a mid-latitude upland environment: weathering, pedogenesis, and geomorphic processes on plutonic rocks (Sila Massif, Calabria). In: Arribas, J., Critelli, S., Johnsson, M.J. (Eds.), Sedimentary Provenance and Petrogenesis: Perspectives from Petrography and Geochemistry. Geol. S. Am. S., pp. 149–166
Schild, M., Siegesmund, S., Vollbrecht, A., Mazurek, M., 2001. Characterization of granite matrix porosity and pore-space geometry by in situ and laboratory methods. Geophys. J. Int. 146, 111–125.
Senkayi, A., Dixon, J., Hossner, L., 1981. Transformation of chlorite to smectite through regularly interstratified intermediates. Soil Sci. Soc. Am. J. 45, 650–656.
Sequeira Braga, M.A., Lopes Nunes, J., Paquet, H., Millot, G., 1990. Climatic zonality of coarse granitic saprolites ("arènes") in atlantic Europe from Scandinavia to Portugal. Sciences Géologiques, bulletins et mémoires 85, 99–108.
Sequeira Braga, M.A., Paquet, H., 1986. Gibbsite as a biotite weathering product in a granitic saprolite from Cavado river basin Northwest Portugal. In: Rodriguez-Clemente, R., Tardy, Y. (Eds.), International Meeting in Geochemistry of the Earth Surface and Processes of Mineral Formation, pp. 175–186. Granada (Spain).
Sequeira Braga, M.A., Paquet, H., Begonha, A., 2002. Weathering of granites in a temperate climate (NW Portugal): granitic saprolites and arenization. Catena 49, 41–56.
Sheldon, N.D., Tabor, N.J., 2009. Quantitative paleoenvironmental and paleoclimatic reconstruction using paleosols. Earth Sci. Rev. 95, 1–52.
Slatt, R.M., Eyles, N., 1981. Petrology of glacial sand: implications for the origin and mechanical durability of lithic fragments. Sedimentology 28, 171–183.
Soil Science Glossary Terms Committee, 2008. Glossary of soil science terms. Soil Sci. Soc. Am. 1–84.
Speer, J., 1984. Micas in igneous rocks. In: Bailey, S. (Ed.), Micas. Min. Soc. Am., pp. 299–349. Washington D.C.
Środoń, J., 1999. Use of clay minerals in reconstructing geological processes: recent advances and some perspectives. Clay Miner. 34, 27–37.
Stoch, L., Sikora, W., 1976. Transformations of micas in the process of kaolinitization of granites and gneisses. Clay Clay Miner. 24, 156–162.
Stolt, M.H., Baker, J.C., 1994. Strategies for studying saprolite and saprolite genesis. Whole regolith pedology. Soil Sci. Soc. Am. S. 34, 1–19.
Stoops, G., Altemüller, H.-J., Bisdom, E.B.A., Delvigne, J., Dobrovolsky, V.V., Fitzpatrick, E.A., Paneque, G., Sleeman, J., 1979. Guidelines for the description of mineral alterations in soil micromorphology. Pedologie 29, 121–135.
Stoops, G., Delvigne, J., 1990. Morphology of Mineral Weathering and Neoformation. II Neoformations. Dev. Soil Sci. Elsevier, pp. 483–492.
Stoops, G., Marcelino, V., Mees, F., 2010. Interpretation of Micromorphological Features of Soils and Regoliths. Elsevier, p. 720.
Taboada, T., Garcia, C., 1999. Pseudomorphic transformation of plagioclases during the weathering of granitic rocks in Galicia (NW Spain). Catena 35, 291–302.
Tan, P., 2014. Clay Mineralogical Studies of Potential Mesozoic Weathering Profiles in Scandinavia-Field Analoguues for Offshore Reservoir Rocks. Department of Geosciences. University of Oslo, Oslo, p. 85.
Tan, P., Oberhardt, N., Dypvik, H., Riber, L., Ferrell Jr., R.E., 2017. Weathering profiles and clay mineralogical developments, Bornholm, Denmark. Mar. Petrol. Geol. 80, 32–48.
Tansi, C., Gallo, M.F., Muto, F., Perrotta, P., Russo, L., Critelli, S., 2016. Seismotectonics and landslides of the crati graben (Calabrian Arc, southern Italy). J. Maps 12, 363–372.
Thiry, M., Schmitt, J.-M., Simon-Coinçon, R., 1999. Problems, progress and future research concerning palaeoweathering and palaeosurfaces. In: Thiry, M., Simon-Coinçon, R. (Eds.), Palaeoweathering, Palaeosurfaces and Related Continental Deposits, pp. 1–17.
Thompson, S., 1994. Fission-track analysis of the crystalline basement rocks of the Calabria Arc, southern Italy: evidence of Oligo-Miocene late orogenic extension and erosion. Tectonophysics 234, 331–352.
Trice, R., Hiorth, C., Holdsworth, R., 2019. Fractured Basement Play Development on the UK and Norwegian Rifted Margins. Geol. Soc., London. S 495.
Van Dijk, J., Bello, M., Brancaleoni, G., Cantarella, G., Costa, V., Frixa, A., Golfetto, F., Merlini, S., Riva, M., Torricelli, S., 2000. A regional structural model for the northern sector of the Calabrian Arc (southern Italy). Tectonophysics 324, 267–320.
Van Dijk, J., Scheepers, P., 1995. Neotectonic rotations in the Calabrian Arc; implications for a pliocene-recent geodynamic scenario for the central mediterranean. Earth Sci. Rev. 39, 207–246.
Velde, B.B., Meunier, A., 2008. The Origin of Clay Minerals in Soils and Weathered Rocks. Springer Science & Business Media, p. 406.
Vepraskas, M., Hoover, M., Jongmans, A., Bouma, J., 1991. Hydraulic conductivity of saprolite as determined by channels and porous groundmass. Soil Sci. Soc. Am. J. 55, 932–938.
Vepraskas, M., Kleiss, H., Amoozegar, A., Guertal, W., 1996. Porosity factors that control the hydraulic conductivity of soil-saprolite transitional zones. Soil Sci. Soc. Am. J. 60, 192–199.
von Eynatten, H., Barceló-Vidal, C., Pawlowsky-Glahn, V., 2003. Modelling compositional change: the example of chemical weathering of granitoid rocks. Math. Geol. 35, 231–251.
Webb, H., Girty, G., 2016. Residual regolith derived from the biotite-controlled weathering of Cretaceous tonalite–quartz diorite, Peninsular Ranges, southern California, USA: a case study. Catena 137, 459–482.
Weltje, G.J., Paredis, B., Caracciolo, L., Heins, W.A., 2018. Quantitative analysis of crystal-interface frequencies in granitoids: implications for modelling of parent-rock texture and its influence on the properties of plutoniclastic sands. Sediment. Geol. 375, 72–85.
Westaway, R., 1993. Quaternary uplift of southern Italy. J. Geophys. Res. Solid Earth 98, 21741–21772.
White, A.F., 1995. Chemical weathering rates of silicate minerals in soils. Rev. Mineral. Geochem. 31, 407–461.
White, A.F., Blum, A.E., Schulz, M.S., Vivit, D.V., Stonestrom, D.A., Larsen, M., Murphy, S.F., Eberl, D., 1998. Chemical weathering in a tropical watershed, Luquillo Mountains, Puerto Rico: I. Long-term versus short-term weathering fluxes. Geochem. Cosmochim. Acta 62, 209–226.
Wilamowski, A., 2002. Chloritization and polytypism of biotite in the Łomnica granite, Karkonosze Massif, Sudetes, Poland: stable isotope evidence. Chem. Geol. 182, 529–547.
Wright, E.P., 1992. The hydrogeology of crystalline basement aquifers in Africa. Geol. Soc. London Special Publ. 66, 1–27.
Yang, W., Wang, J., Ma, F., Zhang, Y., Bai, Y., Sun, X., Li, H., Zhang, J., Wang, P., 2020. Characterization of the weathered basement rocks in the Dongping field from the Qaidam Basin, Western China: significance as gas reservoirs. Sci. Rep. 10, 16694.
Zheng, H., Luo, J., Zhang, Y., Feng, J., Zeng, Y., Wang, M., 2021. Geological characteristics and distribution of granite geothermal reservoir in southeast coastal areas in China. Front. Earth Sci. 697.